NTNU

Norwegian University of
Science and Technology

Real Time Impedance identification of Li-Polymer Battery with Kalman Filter

Ørjan Gjengedal

Master of Science in Cybernetics and Robotics
Submission date: November 2017
Supervisor: Marta Maria Cabrera Molinas, ITK

Norwegian University of Science and Technology
Department of Engineering Cybernetics

Abstract

In a study of a new and an aged lithium-polymer battery cell, a joint Unscented Kalman Filter coupled with a non-linear equivalent circuit battery model formed the basis for on-line identification of the battery impedance characteristics. In order to evaluate estimated impedance parameters produced by the Kalman filter under real racing conditions, a case study using a dynamic drive-cycle for the Revolve NTNU electric race car were developed. Specifically, the cell model developed describes the non-linear relationship between the open-circuit voltage and the battery State-of-Charge (SoC), the ohmic resistance, the non-linear dependency of the charge-transfer resistance on the faracaic current, and a simplified RC-network to describe the diffusion phenomenon. To verify the consistency of the estimated parameters, an impedance characteristic map was constructed at various levels of SoC and isothermal conditions for the new and aged cells using an industrial grade electrochemical impedance spectroscopy device. Moreover, DC-resistance characterization was conducted to support the analysis. In addition, to avoid introducing errors to the system, the nominal capacity of the respective cells were characterized.

Given imposed sampling conditions and load-dynamics, the respective impact of the ohmic resistance and the non-linear charge-transfer dynamics on the overvoltages, was difficult to separate due to the fast electrode kinetics of the cells at temperatures above $25°C$. As a result, the estimated impedance parameters describing the rapid cell dynamics were poorly conditioned on the voltage measurements. As a proof of concept, a simplification was introduced in order to verify the impact of a model-reduction. The results indicated a similar estimation performance with respect to the expected mean of the sum-of-resistances, but with a higher confidence in its inferred value. Thus, for the considered lithium-polymer battery cells operated at cell temperatures above $25°C$, the concatenation of ohmic resistance and charge-transfer dynamics into a single series resistance is likely to be the best candidate to describe the battery State-of-Health (SoH) in terms of their impedance characteristics. The outcome of the simplification is reduced computational effort due to model reduction, and increased confidence in the inferred sum-of-resistance by allowing the series resistance to represent both passive and active electrochemical effects. However, the estimation error for the aged cell with respect to impedance characteristics at low SoC, still persists. This is probably related to limited diffusion, which is not captured with the given Kalman filter decision variables, in addition to assumptions of how impedance parameters evolve in time.

Moreover, secondary results showed that SoC can be estimated very accurately for the new cell, with a maximum estimation error of about 1%. However, due to non-modelled phenomena such as electrochemical hysteresis and thermal dependency on the open-circuit voltage, the SoC estimates for the aged cell was biased in the range of 2-4%. The ultimate purpose of identifying the impedance is to monitor on-line the SoH of the lithium-polymer batteries in a consistent manner over the expected battery lifetime. Emphasizing minimum computational effort and satisfactory reliability, method verification suggest that interrelated phenomena with significant influence on the equilibrium conditions and impedance characteristics at low SoC need to be further explored.

Sammendrag

I en undersøkelse av et nytt og et gammelt litium-polymer batteri ble et joint Unscented Kalman filter kombinert med en ikke-lineær ekvivalentkrets batterimodell grunnlag for identifikasjon av batterienes impedansegenskaper i sann tid. For å evaluere estimerte impedansparametere produsert av Kalman-filteret under reelle kjørebetingelser, ble det utviklet en case study ved hjelp av en dynamisk kjøresyklus for en Revolve NTNU elektrisk racerbil. Spesifikt beskriver den utviklede cellemodellen det ikke-lineære forholdet mellom åpen kretsspenning og batteriets restkapasitet (SoC), ohmsk motstanden, den ikke-lineære avhengigheten av ladningsoverføringsmotstanden på faraday-strømmen, og et forenklet RC-krets for å beskrive diffusjon-fenomenet. For å verifisere samsvar mellom estimerte verdier og målte verdier, ble et karakteristisk impedanskart konstruert ved forskjellige nivåer av SoC og isotermiske betingelser for ny og gammel celle ved bruk av et elektrokjemisk impedansspektroskopiinstrument av industriell karakter. Dessuten ble det utført karakterisering av DC-resistens for å støtte analysen. I tillegg, for å unngå å introdusere feil til systemet ble den nominelle kapasiteten for de respektive cellene karakterisert.

Gitt pålagte prøvetakningsbetingelser og lastdynamikk, viste det seg at effekten av henholdsvis ohmsk motstand og ikke-lineære ladningsoverføringsdynamikk på overspenningen var vanskelig å skille på grunn av cellens hurtige elektrodekinetikk ved temperaturer over $25°C$. Som et resultat, var de estimerte impedansparameterne som beskriver den hurtige celledynamikken dårlig betinget av spenningsmålinger. Som et bevis på konseptet, ble en forenkling innført for å verifisere virkningen av en modellreduksjon. Resultatene indikerte en lignende estimeringsytelse i forhold til det forventede gjennomsnittet av summen av resistansene, men med høyere troverdighet i utledet verdi. For de undersøkte litium-polymer batteriene brukt ved celletemperaturer over $25°C$, vil således sammenkoblingen av ohmsk motstand og ladningsoverføringsdynamikk til en enkelt serie-motstand trolig være den beste kandidaten til å beskrive batteriets helse (SoH) med hensyn til deres impedansegenskaper. Resultatet av forenklingen er redusert beregningsinnsats på grunn av modellreduksjon og økt tillit til den utledete summen av motstand ved å tillate serie-motstanden til å representere både passive og aktive elektrokjemiske prosesser. Imidlertid er estimeringsfeilen for den eldre cellen med hensyn til impedansegenskaper ved lav SoC, fortsatt tilstede. Dette er sannsynligvis knyttet til begrenset diffusjon, som ikke fanges med de angitte avgjørelsesvariablene for Kalman filteret, i tillegg til antagelser om hvordan impedansparameterne utvikler

seg over tid.

Videre viste sekundære resultater at SoC kan estimeres svært nøyaktig for den nye cellen, med en maksimal estimeringsfeil på cirka 1%. På grunn av ikke-modellerte fenomener som elektrokjemisk hysterese og termisk avhengighet av åpen kretsspenning, viste SoC-estimatene for den gamle cellen imidlertid en bias i størrelsesorden på 2-4%. Det endelige formålet med å identifisere impedansen er å overvåke litium-polymer batterienes helse i sann tid på en konsistent måte og over forventet levetid. Ved å vektlegge minimum beregningsinnsats og tilfredsstillende pålitelighet foreslår den utførte metodeverifisering at samvirkende fenomener med signifikant innflytelse på likevektsbetingelsene og impedansegenskapene ved lav SoC må undersøkes nærmere.

Preface

Being a member of the student organization Revolve NTNU for two years have been an inspiring and educational journey, and challenging with respect to patience and endurance.

Professor Marta Molinas introduced me to Kalman filtering as a tool to estimate the battery State-of-Charge (SoC). In 2016, I submitted a technical report on battery modeling and Kalman filter-based State-of-Charge estimation for a race car application. In May 2017, I got the opportunity to present the project work as a scientific paper at the 14th IEEE Int. Conf. on Networking, Sensing and Control, with prof. Marta Molinas and Senior Scientist Dr. Preben J.S. Vie as co-authors. In continuation, prof. Marta Molinas encouraged me to address the challenges of tracking battery impedance in an operating battery cell as a topic for my Master thesis work.

In a study of a new and an aged lithium-polymer battery cell, a joint Unscented Kalman Filter coupled with a non-linear equivalent circuit cell model formed the basis for on-line identification of the battery impedance characteristics. In order to evaluate estimated impedance parameters produced by the Kalman filter under real racing conditions, a case study using a dynamic drive-cycle for the Revolve NTNU electric race car was developed. However, since complex electrochemical processes that depend on conditions such as SoC, temperature, applied current, and age, govern the impedance characteristics, I decided to extend the given objectives to include estimation of SoC. The reliability of most battery management system functions depends on its ability to track the battery SoC and impedance characteristics, and more importantly, in a consistent manner over the expected battery lifetime.

Access to laboratory facilities was provided by Institute for Energy Technology (IFE), Kjeller, a sponsor of Revolve NTNU. The cell tests were conducted at the IFE Battery Material Laboratory, and includes electrochemical impedance spectroscopy, DC-resistance characterization, open-circuit voltage and capacity characterization, and a dynamic drive-cycle. Senior Scientist Dr. Preben J.S. Vie gave training and guidance in operating the electrochemical impedance spectroscopy instrument. All experiments were planned by me, however, due to laboratory regulations, the different instrumental setups were programmed by Dr. Vie.

A Formula Student license of MATLAB was used for implementation of the Kalman filter, cell test data preprocessing, and data analysis. IFE provided EC-LAB, the software for running EIS experiments on the Biologic VSP instrument,

in addition to LifeTest, the software for running all other tests on PEC-ACT0550 battery cell cycler/tester.

The outcome of the thesis work should be useful for Revolve NTNU. Hence, the outline of this thesis is somehow different from the common template. Relevant scientific theory and methods described in literature are elaborated on. These are methods that gave the point of departure in model development in the present work. Throughout the model development, I have proposed some modifications to better describe the dependency between some impedance parameters. I have tried to the best of my abilities to distinguish clearly between own contributions and carefully referred to use of other sources. Most of the referred literature in the bibliography has been selected by me.

Acknowledgments

First and foremost, I would like to thank Professor Marta Maria Cabrera Molinas for her support and guidance to this Master thesis. You showed me trust and gave me the opportunity to work independently. I am grateful for your patience.

I sincerely appreciate the hospitality the employees at Institute for Energy Technology (IFE) showed me. A special thanks to Senior Scientist Dr. Preben J.S. Vie. You trusted me to conduct the cell tests. Without the lab-graded equipment made available, and the support and guidance from you, most of the laboratory experiments would have been difficult, if not impossible, to conduct.

I will miss the companionship in Revolve NTNU. Without the experience I have earned through my work in Revolve, I would never achieved the practical insight with respect to engineering, and the great experience working towards a common goal.

Lastly, I would like to express my deepest gratitude to my beloved partner Kine for your patience and your unselfish support throughout the Master thesis work and my endless commitment to Revolve NTNU.

Ørjan Gjengedal
Trondheim, November 2017

Abbreviations and definitions

4WD	Four-wheel drive
Battery pack	A number of cells connected in parallel and/or series
BEV	Battery Electric Vehicle
BMS	Battery Management System
C-rate	A measure of the rate at which a cell is discharged relative to its nominal capacity
Capacity fade	Aging mechanism related to loss of available capacity
Cell	A single electrochemical unit
Cut-off voltage	Manufacturer specified minimum voltage
EKF	Extended Kalman Filter
ESC	Enhanced Self-Correcting cell model
HEV	Hybrid Electric Vehicle
JUKF	Joint Unscented Kalman Filter
LCO	Lithium Cobalt Oxide ($LiCoO_2$)
Li-ion	Lithium-ion
LiPo	Lithium-polymer

Nominal capacity	The quantity of charge, in ampere-hours a cell is rated to hold
OCV	Open-circuit voltage
Over-charge	Charging a cell above manufacturer specified maximum voltage
Over-discharge	Discharging a cell below manufacturer specified minimum voltage
Over-heating	Heating a cell above manufacturer specified maximum temperature
Power fade	Aging mechanism typically related to increase in battery impedance
Relaxation phase	A phase in which a cell is *relaxing* towards the open-circuit voltage after being subjected to a current
Safe operating area	A specific range of conditions over which the battery cell is allowed to operate without exceeding the manufacturer specified limits of cell voltage, temperature and charge/discharge currents.
SEI	Solid electrolyte interface
SoAP	State of Available Power
SOC	State of charge
SoF	State of Function
SOH	State of health
Thermal runaway	Uncontrolled thermal development (self heating) inside the battery cell
Total capacity	Total amount of charge, in ampere-hours, a cell can hold

List of Figures

Table of Contents

Chapter 1

Introduction

Over the past few decades, lithium-ion batteries has increasingly emerged as one of the key technologies to power future electric systems due to high energy density and high coulombic efficiency [29, 33]. Changing environmental conditions and increasing fossil fuel prizes serve as political and economical driving forces to reduce fuel emissions and dependency on oil [29]. Especially, increasing electric mobility by integrating lithium-ion technology into e.g. Battery Electric Vehicles (BEV) and Hybrid Electric Vehicles (HEV) has become a significant field of interest.

Although lithium-ion batteries offers a promising solution to increase electric mobility, the technology has several, potentially hazardous, disadvantages. Some of these issues concerns increasing cycle and calendar life, performance under extreme temperatures (e.g. below $0°C$), and safety. Lithium-ion cells are sensitive to abusive conditions [24] such as over-charge, high-rate charging and over-heating, which may lead to the onset of possible failure mechanism such as internal short circuiting and uncontrolled thermal development (thermal runaway) to name but a few. Consequently, lithium-ion cells must be kept within their respective "safe operating area", which is defined in the manufacturer datasheet.

1.1 Battery management and monitoring

Justified by the aforementioned safety issues, lithium-ion battery cells need to be monitored and controlled by a battery management system (BMS). To prevent any of the cells from being subjected to abusive conditions, the BMS is often required to perform the following tasks:

1. Measure cell current, voltages, and temperatures.
2. Perform safety controls, e.g. activating shutdown, precharge, and charging control.
3. Perform power, energy, and thermal management during operation.
4. Monitor internal battery parameters, e.g. State-of-Charge, impedance, and State-of-Health.
5. Compute advanced predictive algorithms, e.g. available power, remaining driving range, remaining useful life.

Monitoring of internal battery characteristics that describe the cells present operating conditions [11, 38], are one of the most challenging requirements. Primarily, due to complex electrochemical processes that are governing the non-linear relationship between measureable quantities and the internal battery parameters. Figure 1.1 illustrates a typical dependency chart between BMS monitoring functions.

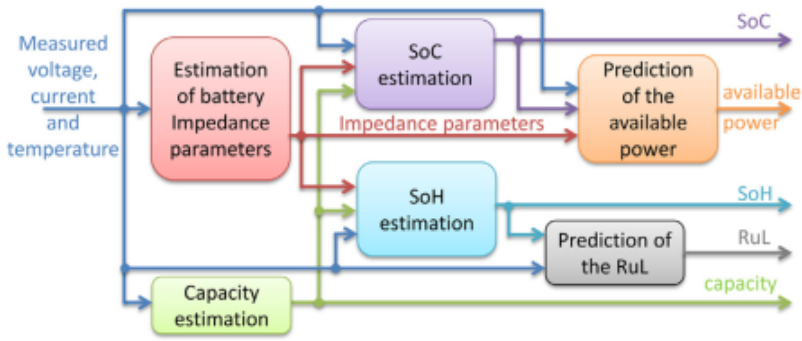

Figure 1.1: A typical interaction diagram between battery monitoring algorithms [38].

State-of-Charge (SoC) indicates the residual capacity relative to the total (or nominal) capacity of the cell [11]. Since no physical sensors exist to measure the SoC directly, the BMS needs to estimate its value from available measurements such as current, voltage and temperature.

The battery impedance defines the overvoltages caused by a passage of a charge or discharge current. Unfortunately, characterizing the battery impedance during

operation is a difficult task due to a number of reasons. For instance, the battery impedance is governed by complex electrochemical processes that depend on the present internal and external conditions such as SoC, temperature, applied current, and age [31].

State-of-Function (SoF) is often referred to the batteries ability to fulfill a particular duty under various conditions [38]. For instance, a duty could be the batteries' ability to provide the necessary energy for a vehicle to reach a certain destination (remaining driving range), or it could be the batteries' ability to accept regenerative energy during breaking or deliver the power needed during propulsion over certain amount of time (prediction of available power). The reliability of the latter strongly depends on the present impedance characteristics.

Due to ageing, the batteries' ability to store energy and provide power to the load decreases over the battery lifetime. State-of-Health (SoH) is a metric for evaluating a battery's ageing level [46], with purpose to track ongoing degradation, e.g. due to cycling, and sudden degradation, e.g. due to abuse. Even though the importance of SoH is evident for prolonging battery life and to enhance safety, its definition is rather vague. Possibly due to the complexity of the aging phenomena, which are still poorly understood [35, 14]. Hence, reaching a general accepted standard for how to determine the SoH of a battery is difficult. In general, the trend over the battery lifetime is that the impedance increases[1], while capacity decreases[2], and are thus often included as SoH metrics [38].

1.2 Research objectives

Since the reliability of most BMS functions depends on having accurate knowledge of the present battery impedance characteristics, this formed the point of departure for the research objective in the present work. However, since the given method employed herein also depends on SoC, the estimation of SoC have been included to extend the given objectives. The ultimate outcome of the work is to identify metric(s) of importance to the battery State-of Health.

[1] Power fade
[2] Capacity fade

Primary research objective

To identify in real time the impedance of a Li-polymer Battery for a Revolve NTNU electric race car using Kalman Filter.

Secondary research objective

- Develop a case study using a dynamic drive-cycle for the Revolve NTNU electric race car
- Evaluate the estimated impedance parameters produced under real racing conditions by comparison with data obtained using Electrochemical Impedance Spectroscopy and DC-resistance characterization
- Track the battery SoC

1.2.1 Estimation of battery impedance - State-of-the-Art

The optimal approach to estimate battery impedance in real-time is not so obvious. Several methods have been proposed in literature [38], and these methods can broadly be classified as: (1) active or passive identification methods, and (2) model-based estimation techniques such as Kalman filtering and least-squares methods.

Active and Passive impedance identification

The *active identification* method rely on special circuits for active signal generation to perturb the battery cell in a desired frequency range. The impedance response is then found using a frequency response analyzer. This method is termed Electrochemical Impedance Spectroscopy, and is a commonly used technique in the laboratory to study different electrochemical properties of the cell. Some authors have even suggested active identification for on-line identification in the field [25, 34]. The *passive identification* is similar to the active identification method, but instead of using special circuitry to perturb the cell, the natural current profile already present due to the cells being connected to a load (e.g. an electric motor) is used. The disadvantage of active and passive identification methods, is that they

rely on the assumption of linear time-invariance[40]. As lithium-ion batteries depends on non-linear electrochemical processes, this assumption may not be fulfilled in a particular situation.

Model-based estimation techniques

Different estimation techniques have been employed in literature to estimate SoC and battery impedance characteristics [38, 11, 36]. Some of these are based on a deterministic approach such as least-squares, or machine learning methods such as fuzzy logic and support vector machines, or stochastic methods such as Kalman filtering and Particle filters. The benefit of stochastic methods, is the inclusion of uncertainty in the inferred characteristics. Hence, the BMS can in a statistical sense reason under uncertainty. While the methods for deducting the underlying battery characteristics are different, the common goal is to estimate the desirable quantities by employing a model that describes the dynamics of the battery cell.

In electric vehicles, the most common methods for developing a battery model are reduced-order electrochemical model [42], neural network [44] model, and equivalent circuit models [11, 36].

A reduced-order electrochemical model derived from first-principals, may provide a very accurate cell model. However, acquiring the physical parameters descriptive of the cell characteristics can be both intractable, time consuming, and may not be easily accessible to the non-specialist. Neural networks are often used for modeling nonlinear systems. However, neural networks view the system as a "black box", and do not provide physical insight into the cells. In consequence, these options have not been pursued.

Equivalent circuits have been extensively used in e.g. estimation of battery impedance [37, 30, 39], SoH [12], and SoC [11]. Equivalent circuits are constructed using electrical analogs such as resistors, capacitors, and voltage controlled sources, to describe the electrochemical phenomena. The parameters of the equivalent impedance model, are often determined by electrochemical impedance spectroscopy [3] or system identification methods [21]. However, a problem with equivalent circuits is the lack of uniqueness [20]. That is, several impedance structures may provide a good current-voltage behavior, but are subject to different interpretation on a physical level. Consequently, difficulties arise in how to determine the correct structure of the equivalent impedance model such that the individual electrical elements describe electrochemical properties of the battery cells being considered.

1.2.2 Revolve NTNU

Revolve NTNU is a student organization that each year designs and builds an electric race car to participate in the engineering student competition – Formula Student - developed by the Society of Automotive Engineers (SAE), to give students the opportunity to experience teamwork, design, manufacture and cost aspects of automotive engineering along with time and project management. Team members are challenged to construct a single-seat race car, which will be put to the test against other Formula Student teams at famous racing circuits such as "Silverstone Circuit" in England, "Red Bull Ring" in Austria, and "Hockenheimring" in Germany.

Figure 1.2: Revolve NTNU 2017 4WD electric race car "Eld".

To be successful in the dynamic events at the Formula Student competitions, the electric race car is dependent on having formidable acceleration and agility in addition to being light weight. Consequently, the battery cells used in this particular application are subjected to harsh conditions, such as high current loads and relatively fast thermal development due to the power output requirements to the inverters and motors.

The battery pack consists of several hundred lithium-polymer cells configured in both parallel and in series, and is one of the biggest and most costly components in the electric vehicle. During the system design process, required energy content, power capability and thermal development characteristics plays a significant role in choosing the appropriate battery cell and cell stack topology. Furthermore, design

choices depends on compatibility requirements with other powertrain components such as the electric motors and inverters. Consequently, designing an appropriately sized battery pack can be a difficult matter, and one is often required to "over-engineer" the battery pack to ensure that the battery cells can deliver the required performance during their expected lifetime.

1.2.3 Technological approach

In the present thesis, a joint Unscented Kalman Filter coupled with a non-linear equivalent circuit model derived from a physical perspective is explored to estimate both battery impedance characteristics and SoC simultaneously. The cell model is motivated by modeling concepts found in literature [36, 16] to target specific electrochemical phenomena using a minimum set of impedance parameters. Considering that the given application is an electric race car, a representative dynamic drive-cycle gathered from measurements during real racing conditions, is used as a case-study. Moreover, to accommodate the notion of aging, two lithium-polymer cells with different aging states are included in the investigation to verify possible weaknesses in the given method. These cells have a nominal voltage of 3.7 V, a rated capacity of 6.55Ah, and are composed of a Lithium Cobalt Oxide (LCO) positive electrode, and a graphite negative electrode.

The point of departure for evaluating the battery impedance characteristics produced by the Kalman filter during real racing conditions, was to gather impedance measurement from two commonly used techniques - electrochemical impedance spectroscopy and DC-resistance characterization. The impedance spectroscopy measurements are conducted at several levels of SoC, and at normal and elevated cell temperatures. Utilizing a complex non-linear least-squares optimization algorithm, the parameters related to the applied cell model is extracted from the impedance measurements to produce a reference-map of battery impedance characteristics. The extracted impedance parameters however, only describes the system response close to equilibrium conditions. Since the Revolve battery cells are usually operated quite far from equilibrium conditions, the DC-resistance measurements are utilized to support the evaluation of the estimated impedance parameters.

Chapter 2

Introduction to electrochemistry

This chapter covers some electrochemical phenomena and terminology relevant to both interpretation of electrochemical impedance measurements in Chapter 3 and modeling of lithium-polymer cells in Chapter 4. Specifically, the objective in this chapter is to present lithium-ion/polymer battery cells from a practical perspective to guide the theoretical understanding of how lithium-ion/polymer cells work and what to be aware of in terms of underlying electrochemical phenomena that have impact on its performance.

2.1 Lithium-polymer batteries

Lithium-polymer and lithium-ion cells are insertion-electrode cells that depends on intercalation mechanisms [26, 44, 42]. The cells are built from a number of principal components, which includes porous negative and positive electrodes, electrolyte, separator and current collectors. The cell characteristics depends upon a number of factors, such as electrode material used, and type of electrolyte [42]. The differences between lithium-polymer and lithium-ion cells, is that that lithium-polymer cells use a polymer electrolyte, while lithium-ion cells use a liquid electrolyte.

During discharge, lithium-ions deintercalate from the negative electrode compound and moves through the electrolyte and separator due to mass transfer, and finally intercalate into the lattice of the positive electrode. A schematic of the discharge process is depicted in Figure 2.1. A similar, but reverse, process occurs when charging the cells. For this to work, the electrolyte serves as both an electrical insulator and ionic conducting substance, allowing lithium-ions to flow from

one electrode to the other while the electrons travels through the external circuit.

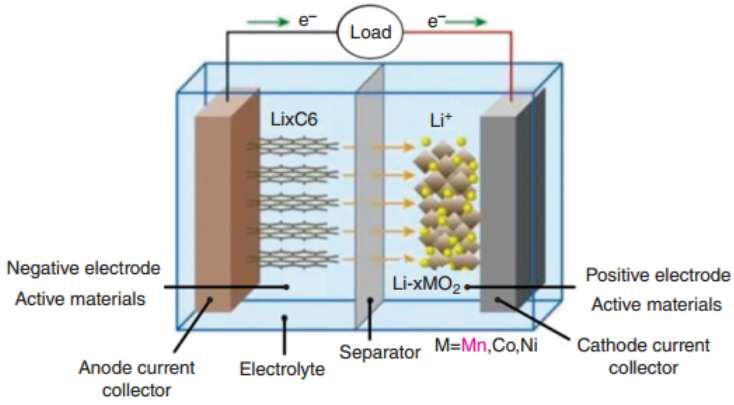

Figure 2.1: Schematic of a discharge process of lithium-ion cells [44].

The positive electrode has high potential and poor lithium state, and the negative electrode has low potential and rich lithium state [44]. Hence, when fully charged, the lithium-ions reside in the lattice of the negative electrode, and when fully discharged the lithium-ions reside in the positive electrode. Fully charged and fully discharged state depends on the electrode materials. The battery cells used in present work have a nominal voltage of 3.7V, rated capacity of 6.55Ah, a lithium cobalt oxide (LCO) positive electrode, and a graphite negative electrode. These cells are fully charged at 4.2 V (V_{max}) and fully discharged at 3.0 V (V_{min}). A more thorough cell specification is given in Appendix B. Moreover, the discharge and charge capability of a cell is commonly governed by its C-rating. A C-rate is a measure of the rate at which the cell is discharged relative to its nominal capacity. To generalize the notion of C-rate, 1C for a cell with 1 Ah nominal capacity should be able to deliver a 1 A discharge current for an hour.

2.2 State-of-Charge

State-of-Charge (SoC) is defined as the ratio of the residual capacity Q_{res} to the total capacity Q_{tot} [42, 43]. Hence, SoC describes a cells' present "charge status" by the following relationship,

$$SoC(t) = \frac{Q_{rem}(t)}{Q_{tot}} \tag{2.1}$$

where $SoC(t) \in [0\%, 100\%]$ (or [0,1]), and Q_{tot} (in Ampere-hours) is the total cell

capacity, which must be characterized in order to determine when a cell is fully charged and fully discharged.

In general, the total cell capacity Q_{tot} is not known [43], because the amount of charge that can be drawn from the cell is dependent on several factors such as the rate of discharge, temperature, and the cut-off voltage V_{min}. Using a high discharge rate will increase the cell polarization due to impedance, which results in the cell reaching the cut-off voltage sooner, and the amount of charge drawn from the cell will be lower. Consequently, the capacity that a cell is rated to hold is typically characterized under nominal conditions, often predefined by the manufacturer. For the cells studied in the present work, the rated capacity can be found in the datasheet in Appendix B. However, the present work will utilize the definition in Plett [11] to characterize the nominal capacity of the respective cells in this study, as it is assumed to be closer to the total capacity of the cells.

Definition of nominal capacity

The nominal capacity Q_n of a cell is the number of ampere-hours that can be drawn from a cell at room temperature at a constant current C/30 rate, starting with the cell fully charged [11].

A popular method for estimating SoC, when the nominal capacity is known, is the Coulomb Counting (or ampere-hour counting) method defined as [44],

$$\begin{aligned} SoC(t) &= \frac{Q_{res}(t)}{Q_{tot}} \\ &\approx \frac{Q_{res}(t)}{Q_n} \\ &= SoC_{t_0} + \frac{\Delta Q(t)}{Q_n} \\ &= SoC_0 + \frac{\int_{t_0}^{t} I(\tau)\tau}{Q_n} \end{aligned} \tag{2.2}$$

where SoC_{t_0} is the initial SoC at time t_0, and $I(t)$ is the instantaneous cell current at time t.

With the above definition, SoC changes only due to a passage of current. There are however, some processes that affects the change of SoC, which isn't described in the Coulomb Counting method in Equation 2.2. These include *self-discharge*

and *coulombic efficiency.*

Self-discharge is defined as the percentage of capacity that a cell looses in its open-circuit condition [45], and involves any transport of electrons across the electrolyte. Consequently, this results in loss of SoC even if the cell is unloaded.

Coulombic efficiency[1] is a ratio between the amount of charge drawn from the cell during a discharge cycle and the amount charge that enters the cell during a charge cycle,

$$\varepsilon_{eff} = \frac{Charge\ out}{Charge\ in} \tag{2.3}$$

and is related to parasitic or unwanted side reactions occurring in the cell, such as loss of lithium inventory due to the growth of the solid electrolyte interface [45]. For instance, when charging a cell, most of the lithium-ions participates in raising the cells' SoC. However, due to unwanted side reactions, a fraction of the lithium-ions are bonded (immobilized) and do not increase the cell's SoC.

2.3 Open-circuit voltage

When a cell is disconnected from an external circuit, the cell is said to be in *open-circuit voltage* condition. This entails that no current passes "through" the cell, and that a cells terminal voltage has been allowed to rest to electrochemical equilibrium. The latter implicates, from an electrochemical point of view, that lithium-ions in the electrolyte are in equilibrium with lithium intercalated into the lattices of the respective electrodes (Figure 2.1).

There is a close relationship between OCV and SoC. That is, the OCV of an electrochemical cell displays a nonlinear dependence on cell SoC, as depicted in Figure 2.2. According to Plett [42], the open-circuit voltage also has a slight dependency on temperature.

[1] The symbol η is used elsewhere [11] to represent the Coulombic efficiency. However, η is often used to represent overpotentials, and thus ε is used here to represent Coulombic efficiency to avoid ambiguity.

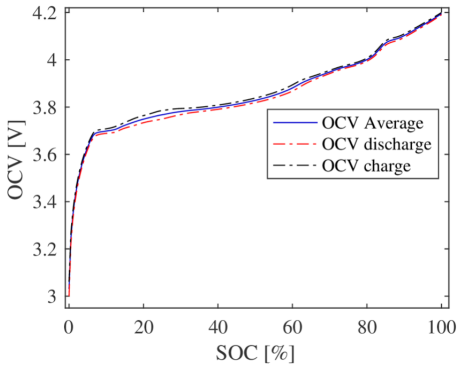

Figure 2.2: Open-circuit voltage (OCV) vs State of Charge (SoC). Established in previous work [48, 49] at $25°C$.

2.4 Electrochemical Impedance

The impedance in an electrochemical cell is commonly associated with ohmic resistance, charge transfer and interfacial charging at the electrode interface, and mass transfer processes [36]. As a result of it's impedance, the measured voltage of an electrochemical cell experiences overvoltages due to a passage of current:

$$V(t) = ocv(SoC(t)) - R_{ohmic}I(t) - \eta_{ct}(t) - \eta_{diff}(t) \tag{2.4}$$

where $V(t)$ and $I(t)$ are the measured cell terminal voltage and cell current respectively, and $R_{ohmic}I(t)$, $\eta_{ct}(t)$ and $\eta_{diff}(t)$ are overvoltage[2] contributions due to ohmic resistance, charge-transfer reactions, and diffusion. The latter is assumed to be the dominant mode of mass-transfer, which according to Ratnakumar *et. al* [15] is quite probable due to slow diffusion-rates of lithium-ions in the respective lattice of the electrodes. The impact of the overvoltages on the departure from the open-circuit voltage condition is illustrated in Figure 2.3.

[2]Or polarization voltages

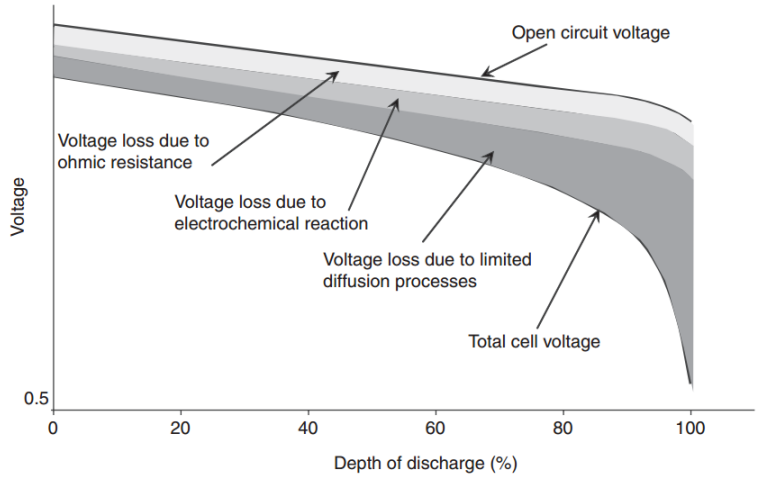

Figure 2.3: Voltage curve during discharge, illustrating the effect of different voltage losses starting from the open-circuit voltage [22]. Depth of discharge = 100 − State of Charge (%).

2.4.1 Ohmic resistance

The ohmic resistance is caused by a number of factors. These include ionic resistance due to the electrolyte, and electronic resistances due to electrodes, current collectors and other contact resistances [7, 15, 22]. Furthermore, the ohmic resistance is in general not a result of chemical reactions, but it may change slightly to changes in SoC due to variations in the electronic resistance in the electrodes [15]. While the resistance in electronic conductors increases with increasing temperature, and the ionic resistance in the electrolyte decreases with increasing temperature [22]. Typically, the ohmic resistance is mostly influenced by the resistance in the electrolyte, and the overall ohmic resistance is thus expected to decrease with increasing temperature. Consequently, the over-voltage caused by the ohmic resistance produces a constant voltage drop or rise depending on the direction of the applied current, and varies with changing temperature conditions.

2.4.2 Intercalation reactions

The overvoltage associated with an activation controlled charge transfer reaction, which occurs during intercalation, is often expressed through the Butler-Volmer equation [36]:

$$I_f = Ai_0(e^{\frac{\alpha_a F}{RT}\eta_{ct}} - e^{-\frac{\alpha_c F}{RT}\eta_{ct}}) \tag{2.5}$$

where I_f is the faradaic current produced by the reaction, and η_{ct} is the activation overpotential occurring at the respective electrode. The exchange current density i_0 ($\frac{A}{cm^2}$) describes the stiffness of the reaction [36]. For a large valued i_0, the overpotentials changes only moderately. A is the active surface area of the respective electrode. The "symmetry" of the overpotential for anodic or cathodic reactions, are determined by α_a and α_c respectively, where the anodic and cathodic transfer coefficients must satisfy $\alpha_a + \alpha_c = 1; \alpha_a, \alpha_c \geq 0$. F is the Faraday constant, R is the universal gas constant, and T is the absolute temperature given in Kelvin.

The intercalation reaction has a certain resistance to it, which is commonly known as the charge-transfer resistance [37]:

$$R_{ct} = \frac{\eta}{I_f} \tag{2.6}$$

Due to the non-linear nature of the Butler-Volmer Equation 2.5, the corresponding current-voltage behavior results in a non-linear change in charge-transfer resistance depending on the amplitude of the faradaic current I_f [37]. The effect is shown in Figure 2.4.

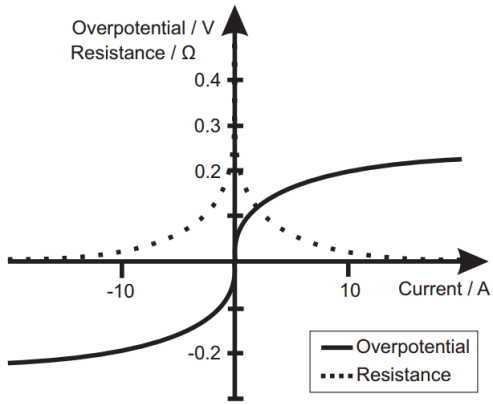

Figure 2.4: Overpotential and resistance change caused by the Butler-Volmer kinetics. Fleischer *et. al* [37] referring to Dyer *et. al* [27]. Valid for transfer coefficients $\alpha_a = \alpha_c = 0.5$.

The faradaic current dependency on the charge-transfer reaction is reported by Waag *et. al* [30] to be substantial at low temperatures and as battery aging progresses.

2.4.3 Diffusion

Diffusion is a complex phenomenon, which describes the movement of charged species (e.g. lithium-ions) from a location with high concentration to another location with low concentration. The driving force for movement of charged species is a concentration gradient, which occurs between the surface of an electrode and the bulk of the electrolyte [22]. As a result of the concentration gradients, a diffusion overvoltage η_{diff} occurs. According to Sauer [22], the diffusion overvoltage is increasingly pronounced when high current rates are applied. Due to limited diffusional rates, the concentration gradients increases and results in addiotanl overvoltages which can limit the performance of the cell.

Chapter 3

Electrochemical impedance spectroscopy

Electrochemical impedance spectroscopy (EIS) is a common technique for measuring the impedance response of an electrochemical system (e.g. a battery) as it gives useful insight into the kinetic and transport properties [5, 6]. This technique involves applying a small AC perturbation signal (current or voltage) to an electrochemical cell at different frequencies, measuring the system's response (current or voltage), and determining the complex impedance using Fourier transformation and Ohm's law. The result is the impedance spectra of the electrochemical cell around a particular working point (SoC, temperature, age). Two modes of operation are commonly used for perturbation in EIS experiments, known as galvanostatic mode and potentiostatic mode. In galvanostatic mode, current is used as the perturbation signal and the voltage response is recorded. In potentiostatic mode, voltage is used as the perturbation signal and the current response is recorded.

EIS relies on the electrochemical cell to behave like a linear time-invariant system[1] during the experiment [5]. Due to the non-linear nature of battery cells, small perturbation signals are used in order for these requirements to be met. Particularly, at low frequencies the sinusoidal excitation can take several minutes, thus changing the cell temperature or SoC if the signal amplitude is too large over the duration of measurement.

[1] Or at least like a quasi-linear and quasi-stationary for the time of measurement [5]

3.1 Interpretation of EIS - The Randles Circuit

The challenge of analyzing the impedance characteristics of a battery is that the electrochemical processes of both electrodes blend together to form the total impedance response. This complicates the interpretation of the underlying mechanisms that contributes to the measured impedance spectra because it is impossible to separate the positive and negative electrode processes that occurs at very similar time-constants.

The impedance response is commonly visualized using a Nyquist plot or a Bode plot. A typical impedance response of a lithium-ion battery cell is depicted in a Nyquist plot in Figure 3.1. Nyquist plots are very popular because different shapes visible in the impedance response may be attributed to specific electrochemical processes.

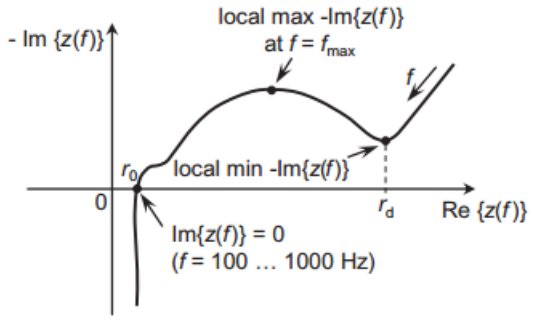

Figure 3.1: Typical complex impedance response of a lithium-ion battery cell [32].

In the Nyquist plot shown in Figure 3.1, the frequency increases from right to left along the real axis. The ohmic resistance (r_0) is observable at the point of intersection with the real axis where the inductive and capacitive impedance's cancel each other. The high-frequency semi-circle (smaller circle) is often argued to be the cause of the solid electrolyte interphase [32], and may or may not be present in the impedance spectra depending on battery condition (SoC, temperature, age). The mid-frequency semi-circle is connected to the charge-transfer process in parallel to the double-layer capacitance. The double layer capacitance occurs due to a phase-transition between the electrodes and the electrolyte. The low-frequency impedance response is characterized by an elongated tail, and is caused by slow diffusion.

Equivalent circuits are often used by electrochemists to better understand the electrochemical processes using EIS measurements. However, a problem with equiv-

alent circuits is the lack of uniqueness. Orazem and Tribollet [20] states that a good fit does not necessarily justify the structure of a model for the underlying processes, as several equivalent circuits may provide an equal impedance response. In general, an equivalent impedance model should contain a minimal set of model parameters to describe the underlying impedance mechanisms in order to reduce the influence of ambiguity when interpreting the impedance spectra. For these reasons, the Randles circuit shown in Figure 3.2 is considered to be a good starting point for an equivalent circuit because it matches most of the underlying impedance mechanisms observed in impedance spectroscopy with a minimum set of model parameters [20].

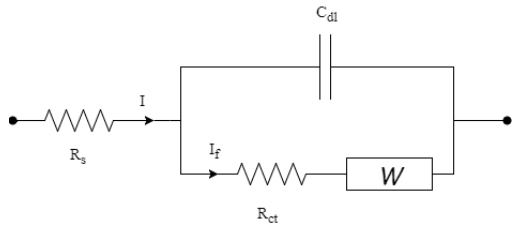

Figure 3.2: Randles circuit.

Specifically, a series resistance R_s is used to describe the ohmic resistance, a capacitance C_{dl} is used to describe the electrical double layer related to the electrode/electrolyte phase boundary, and a charge-transfer resistance R_{ct} in series with a Warburg element W to describe the faradaic impedance. At low frequencies, the faradaic impedance is dominated by the Warburg element. At higher frequencies, the Warburg impedance tends towards zero. Complex Warburg behaviors caused by diffusion processes is demonstrated in Figure 3.3.

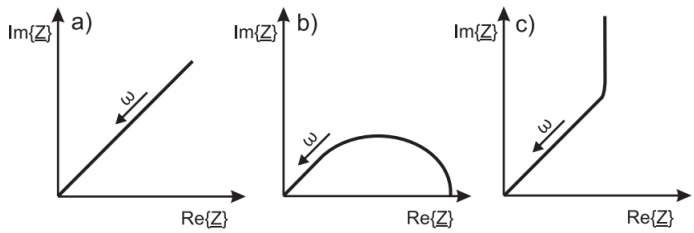

Figure 3.3: Complex impedance caused by diffusion processes with a) quasi-infinite diffusion-length, b) limited diffusion length but unlimited reservoir and c) limited diffusion length with non-permeable wall as boundary [36, 19].

3.2 EIS experiment description

In the present work, a BioLogic VSP with a 4 Ampere booster and a 4-wire measurement setup, was used to record the impedance response of the new and the aged cells. To measure the impedance response at different temperatures, the cells were put in a thermally controlled environment using a Firlabo climatic chamber. The impedance response for both cells have been recorded at $25°C$, $30°C$, $35°C$ and $40°C$.

According to Fleischer *et. al* [36], referring to Pilatowicz [28], use of galvanostatic mode is preferred since a battery cell's SoC could change during the frequency-sweep using potentiostatic mode. This is argued to be caused by different amount of charge being drawn and put into the cell during the positive and negative half-wave of the perturbation signal. Consequently, galvanostatic mode has been selected as the mode of perturbation in the experimental tests.

Different signal amplitudes[2] ranging from 500 mA (at $25°C$) to 1.4 A (at $40°C$) was needed to get sufficiently good signal-to-noise ratio at the different isothermal conditions. Morover, the impedance response was averaged on a set of five measurements per frequency to further reduce the effect of noise. The test procedure is summarized in "EIS test procedure" for easy reference.

[2]Determined by trial and error

EIS test procedure

Step 1:	Preset climatic chamber to test temperature T ($^{\circ}C$). Allow cell to temper.
Step 2:	Fully charge cells using CC-CV* method
Step 3:	Allow cell to temper and equilibrate for 30 minutes
Step 4:	Do EIS experiment with desired settings
Step 5:	Discharge cells by 20% SoC increments. If $V_{cell} < V_{min} \rightarrow$ go to step 6. Else go to step 3.
Step 3:	Allow cell to temper and equilibrate for 45 minutes
Step 6:	Do EIS experiment with desired settings
Step 7:	End

EIS settings

1. Perturbation mode:	Galvanostatic (single-sine)
2. Perturbation amplitude**:	500 mA
3. Frequency range:	10 kHz to 50 mHz
4. Number of points per frequency decade:	20
5. Measurements per frequency (averaging):	5

* Constant-Current Constant-Voltage
**At 25$^{\circ}C$. 750 mA, 1100 mA and 1400 mA have been used at 30$^{\circ}C$, 35$^{\circ}C$ and 40$^{\circ}C$ respectively.

3.3 Experimental investigation of a new and an aged cell

First, the measured impedance spectra is presented and discussed. Due to the amount of measured impedance data, only a selected few are included in the present chapter. However, the complete set of impedance spectra (Nyquist and Bode diagrams) for both cells at all SoC and temperatures can be found in Appendix C. After this, impedance parameters are extracted using a complex non-linear

least-squares optimization technique (*lsqnonlin(·)* in Matlab).

3.3.1 Measured impedance response

Figure 3.4 and 3.5 illustrates the SoC and thermal dependency on the measured impedance spectra for the new and the aged cell.

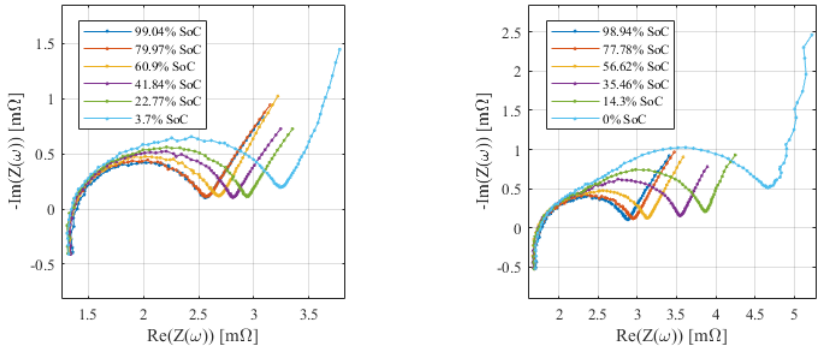

(a) New cell (b) Aged cell

Figure 3.4: EIS at $25°C$ and various SoC. Frequency range from $2000Hz$ to $50mHz$.

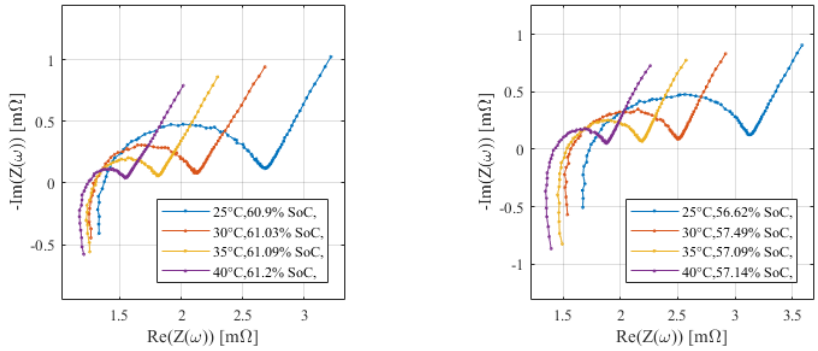

(a) New cell (b) Aged cell

Figure 3.5: EIS at various temperatures. Frequency range from $2000Hz$ to $50mHz$.

In Figure 3.4, the ohmic resistance is observable at the point where the impedance response intersects with the real axis. For the new and the aged cell, this occurs at $Re(Z) \approx 1.4m\Omega$ and $Re(Z) \approx 1.8m\Omega$ respectively. Moreover, the aged cell has roughly 30% higher ohmic resistance compared to the new cell at $25°C$. As can be

seen for both the new and the aged cell in Figure 3.4 and 3.5, the ohmic resistance is fairly independent of SoC, and decreases at elevated temperatures due to increase in electrolyte conductivity. This complies with the theory presented in Chapter 2.

For mid-frequencies in Figure 3.4, the new cell shows a depressed capacitive semicircle, and grows with decreasing state of charge. Contrary to the new cell, the aged cell seems to have a second depressed semi-circle at higher frequencies, and a nearly non-depressed semi-circle at mid-frequencies. This is more pronounced at low SoC. As cell temperature increases, the semicircle(s) decreases remarkably for both cells, as shown in Figure 3.5. Moreover, the semi-circles for the aged cell are gradually overlapping.

At the low-frequency end of the depicted spectra, diffusion becomes visible as an elongated tail with an angle $> 45°$ for both cells. This is somewhat different from the various Warburg behaviors depicted in Figure 3.3. Only a limited amount of information about the diffusion process is given in the spectra down to $50mHz$. Hence, it is not possible to exclude any of the aforementioned Warburg elements.

3.3.2 Model fitting and estimated Randles parameters

The mid-frequency response of the Randles circuit in Figure 3.2 would be kinetically correct for the measured impedance spectra if the semi-circle traced a perfect half-circle with radius $\frac{R_{ct}}{2}$. It would then correspond to a single-step activation-controlled process [20]. However, due to the depressed semi-circle a more detailed model is necessary to describe the impedance response. One way to obtain a better fit is to replace the double layer capacitance with a constant phase element (CPE) [20]. The impedance response of a CPE element is given by:

$$Z_{CPE} = \frac{1}{Qs^{\beta}} \tag{3.1}$$

$$C_{dl} = \frac{(QR_{ct})^{\frac{1}{\alpha}}}{R_{ct}} \tag{3.2}$$

where Q is the CPE coefficient, and β describes capacitance dispersion $\beta \in [0, 1]$. When $\beta = 0$ the CPE behaves like a resistor, and when $\beta = 1$ it behaves like a capacitor. Moreover, when $\beta = 0.5$ it is behaving like the Warburg element shown in Figure 3.3a. The difference between employing a CPE in contrast to an ideal capacitor is illustrated in Figure 3.6, where C_{dl} is inferred from Equation 3.2.

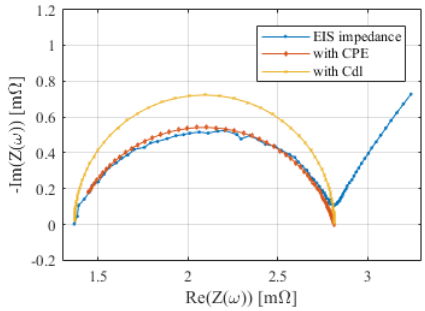

Figure 3.6: Ideal capacitor vs constant phase element using Equation 3.2 to compute the C_{dl}.

There is no clear indication of multiple peaks for the new cell, and is thus treated as a single depressed semi-circle. Clearly, the aged cell requires a more detailed model to describe its impedance response due to the presence of two overlapping semi-circles. Moreover, the "elevated" angle $> 45°$ requires a more detailed explanation than what can be given by the Warburg elements. However, any interpretation of the cause for the angle has been deemed outside the scope of this work. Hence, by disregarding uncertainty consideration, the kinetic treatment of both cells are done with the Randles circuit, where both the double layer capacitance and the Warburg behavior are replaced by a constant phase element.

As a result of the simplifications, only the ohmic resistance and charge-transfer resistance is extracted for reference. For reasons that will be made clear in Chapter 4, the extracted charge-transfer resistance is used for producing reference values for the exchange current, which is related to the Butler-Volmer equation in chapter 2. The results the model fitting, and the extracted parameters are shown in Figures 3.7-3.11.

In hindsight of the simplification, the model fitting and parameter estimation is rather cumbersome. The obtained estimates may have been extracted from directly from the plots (Refering to Figure 3.1). Nevertheless, the obvious advantage is that the estimation is automated.

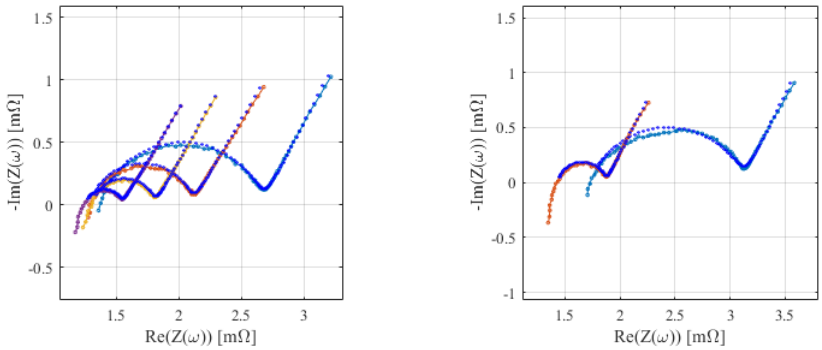

(a) New cell (b) Aged cell

Figure 3.7: Nyquist plot - Model fitting (dark blue). New cell at 60% SoC and various temperatures: $25°C$ (light blue), $30°C$ (orange), $35°C$ (yellow), $40°C$ (purple). Aged cell at 57% SoC and two temperatures only: $25°C$ (light blue) and $40°C$ (orange).

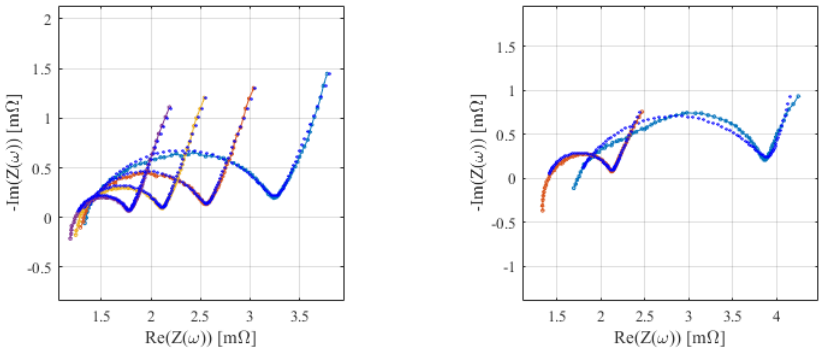

(a) New cell (b) Aged cell

Figure 3.8: Nyquist plot - Model fitting (dark blue). New cell at 3.7% SoC and $25-40°C$. Aged cell at 14% SoC, and $25°C$ (light blue), $40°C$ (orange).

Figure 3.7 depicts the results of model-fitting by the use of a non-linear least-squares optimization technique, using lsqnonlin in Matlab.

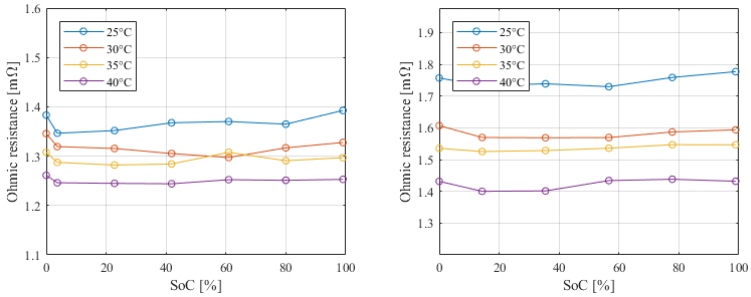

(a) New cell (b) Aged cell

Figure 3.9: Estimated ohmic resistance characteristic map.

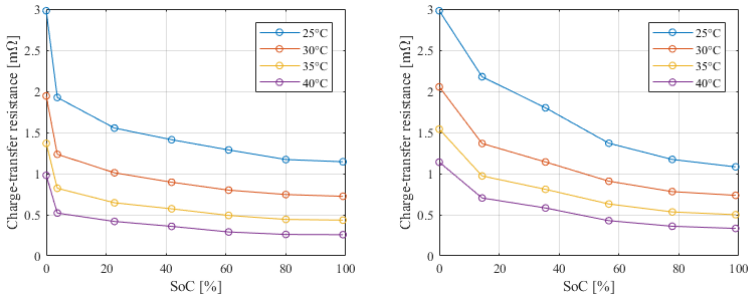

(a) New cell (b) Aged cell

Figure 3.10: Charge-transfer resistance characteristic map.

Assuming that the consireded battery cells comply with the Butler-Volmer Equation 2.5 for an activation controlled process, then the charge-transfer resistance at small signal perturbation can be expressed in the linearized form to extract reference values at equilibrium conditions.

The derivative of the faradaic current with respect to the electrode overpotential is given by:

$$\frac{dI_f}{d\eta} = \frac{I_0 F}{R_g T}(\alpha_a e^{\frac{\alpha_a F}{RT}\eta} + \alpha_c e^{-\frac{\alpha_c F}{RT}\eta}) \tag{3.3}$$

A first-order Taylor expansion of Equation 2.5 around zero overpotential is given by:

$$I_f = I_f(0) + \frac{dI_f}{d\eta}\Big|_{\eta=0}\eta \tag{3.4}$$

$$I_f = \frac{I_0 F}{R_g T}(\alpha_a + \alpha_c)\eta \tag{3.5}$$

$$I_f = \frac{I_0 F}{R_g T}\eta \tag{3.6}$$

remembering that $\alpha_a + \alpha_c = 1$ from Chapter 2. At this point, it is clear that EIS does not allow us to determine the anodic and cathodic transfer-coefficients. Inserting Equation 3.6 into the definition of the charge-transfer resistance 2.6 yeilds:

$$R_{ct} = \frac{\eta}{I_f} \tag{3.7}$$

$$R_{ct} = \frac{\eta}{\frac{I_0 F}{R_g T}\eta} \tag{3.8}$$

$$R_{ct} = \frac{R_g T}{I_0 F} \tag{3.9}$$

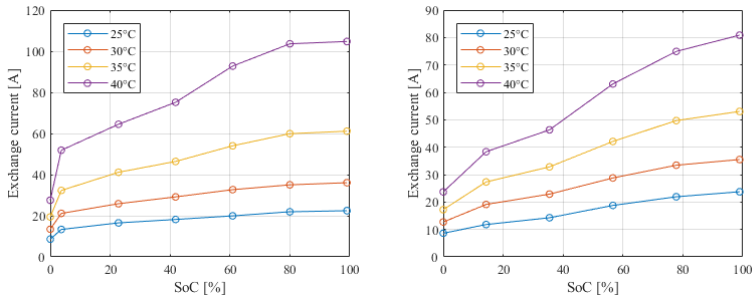

(a) New cell (b) Aged cell

Figure 3.11: Exchange current characteristics map.

3.4 Direct current resistance characterization

Measuring a cell's impedance is dependent on the method of choice. Another common method to determine the impedance of an electrochemical cell is by the use of a DC current-injection or current-interrupt method (see Figure 2.3). The DC-resistance does not fully describe the battery dynamics as predicted by EIS.

However, since the Revolve battery cells are usually operated at conditions far from equilibrium, the DC-resistance will useful to support the evaluation of "correctness" in the case-study in Chapter 6.

The method for measuring the DC-resistance is part of the PEC-ACT0550 battery tester's own programming manual [47]. The DC-resistance is measured by a current-interrupt method, by applying two levels of constant current discharge over a fixed duration of 100 ms:

$$R_{DC} = \frac{V_1 - V_2}{I_1 - I_2} \tag{3.10}$$

where $(V_1,\ I_1)$ and $(V_2,\ I_2)$ are the measurement results at the end of the first 50 ms and the second 50 ms load event respectively. Given the time-scale of the DC-resistance measurement, it is expected to be close to the sum-of-resistances $R_s + R_{ct}$. The results of the measurements are showin in Figure 3.12 and 3.13 for the new and the aged cells.

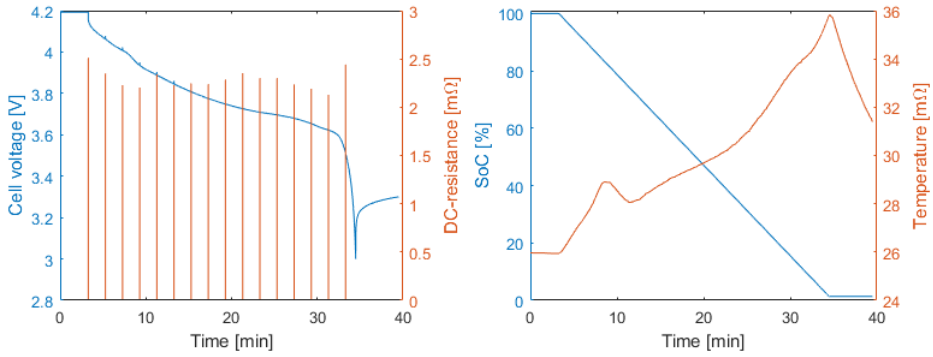

(a) (b)

Figure 3.12: DC-resistance calculation of a new cell based on current-interrupt method: (a) Cell voltage and DC-resistance, (b) SoC and cell temperature

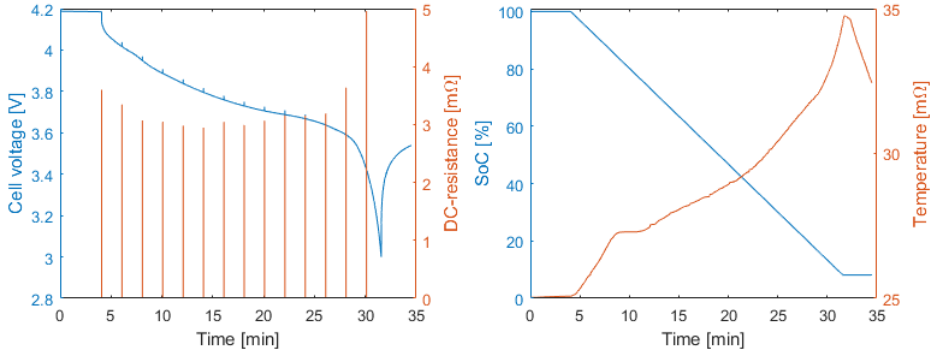

(a) (b)

Figure 3.13: DC-resistance calculation of an aged cell based on current-interrupt method: (a) Cell voltage and DC-resistance, (b) SoC and cell temperature

Chapter 4

Battery modeling

While Chapter 3 presented impedance measurements and a method for interpretation of the impedance response in the frequency domain, the present chapter is concerned with constructing a cell model that can be used as part of the Kalman filtering framework (Chapter 5) in the discrete time-domain.

To enable a Kalman filter to estimate internal battery characteristics and predict the cell voltage during steady-state and dynamic load situations, the cell model equations must account for changes in SoC and dynamic overvoltages due to a passage of current. First, a simple procedure for characterizing the dependence of SoC on the open-circuit voltage is presented. Then, a step-by-step procedure for transforming the Randles-circuit into a simplified equivalent impedance model in the time-domain is given. In contrast to the linearized Butler-Volmer equation 3.9 for small overpotentials, a method for including the non-linear dependence on the faradaic current on the charge-transfer resistance is presented. At the end of this chapter, the complete cell model is summarized.

4.1 Empirical OCV vs SoC

While the overvoltages caused by battery impedance are more dynamic in nature, the OCV is a static function that depends slightly on temperature [42] and non-linearly on SoC. Therefore, it is useful to do a separate battery test to characterize the OCV dependence on SoC and temperature. However, due to time-constraints, only characterization at $25°C$ has been conducted in the present work.

OCV-SoC and capacity test

Starting with fully charged cells, empirical data is gathered at test temperature T ($°C$) by discharging the cells at constant current C/30-rate until fully discharged (V_{min}), and then charging the cells at constant current C/30-rate until fully charged (V_{max}).

The discharge and charge capacity (Equation 4.1 and 4.2) of both the new and aged cell is determined by using the ampere-hour collected data from the discharge and charge curves. Additionally, the Coulombic efficiency can be computed using Equation 4.3. Table 4.1 summarizes the parametric values obtained from the test, and Figure 4.1 displays the difference in discharge capacity for the new and aged cell

$$Q_{discharge} = \text{Total Ah discharged} \tag{4.1}$$

$$Q_{charge} = \text{Total Ah charged} \tag{4.2}$$

$$\varepsilon_{eff} = \frac{Q_{discharge}}{Q_{charge}} \tag{4.3}$$

Table 4.1: Discharge/charge capacity and coulombic efficiency for a new and aged cell

	Discharge capacity (Ah)	Charge capacity (Ah)	Coulombic efficiency (%)
New cell	6.9051	6.9844	98.87
Aged cell	6.5286	6.6699	97.88

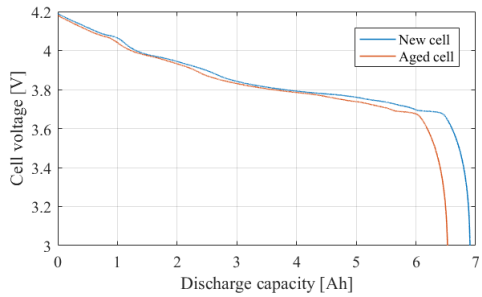

Figure 4.1: Discharge capacity of a new and aged cell at $25°C$ using C/30 discharge rate.

Utilizing the ampere-hour collected data, the SoC is determined by using the Coulomb Counting method in Equation 2.2, assuming fully charged cells (SoC= 1, or 100%) before discharging the cells, and assuming fully discharged cells (SoC= 0, or 0%) before charging the cells. The OCV-SoC relationship is then constructed as the average (See Equation 4.4) of the OCV computed from the discharge and charge curves in 0.5% SoC increments. Hence, creating a 1x201 look-up table[1] which can be used to infer OCV from SoC estimates using linear interpolation and extrapolation.

The result is an approximated OCV-SoC relationship shown in Figure 4.2a. This approach minimizes, to some extent, the influence of overvoltages and hysteresis contributions during the test [21]. The impact of overvoltages and hysteresis is calculated using Equation 4.5, and is shown in Figure 4.2b.

$$OCV_{avg}(SoC) = \frac{OCV_{chg}(SoC) + OCV_{dis}(SoC)}{2} \tag{4.4}$$

$$OCV_{offset}(SoC) = \frac{OCV_{chg}(SoC) - OCV_{dis}(SoC)}{2} \tag{4.5}$$

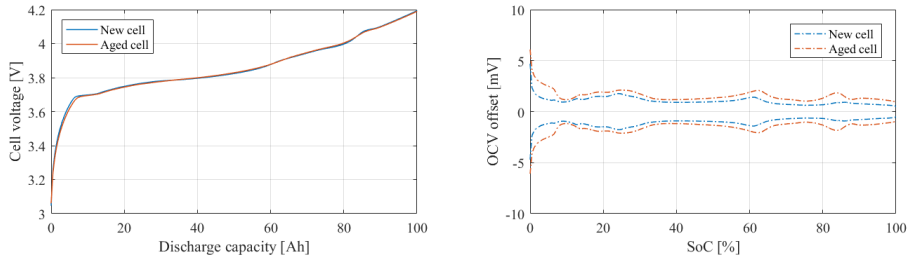

(a) Average OCV vs SoC

(b) Overpotentials and hysteresis

Figure 4.2: Empirical OCV vs SoC of a new and aged cell at $25°C$.

Utilizing the definition of nominal capacity from chapter 2, the nominal capacity of the new and aged cell is 6.9051 Ah and 6.5286 Ah respectively. The Coulombic efficiency can be included in calculation of SoC using the approach suggested by Plett [11]. A continuous-time mathematical description of the SoC rate-of-change can then be modeled as:

[1] Which is easily implemented in a microcontroller with O(1) execution speed for cells having a strictly monotonically increasing OCV as SoC increases.

$$\frac{dSoC}{dt}(t) = -\varepsilon_{eff,i}\frac{I(t)}{3600Q_n} \tag{4.6}$$

where t is time in seconds, $I(t)$ is the instantaneous cell current in amperes (assumed to be positive for discharge, and negative for charge), Q_n is the nominal capacity in ampere-hours[2], and $\varepsilon_{eff,i}$ is the Coulombic efficiency[3] defined as:

$$\varepsilon_{eff,i} = \begin{cases} 1\ , & \text{discharge} \\ \varepsilon_{eff}\ , & \text{charge} \end{cases} \tag{4.7}$$

Assuming a suitably small time step Δt, and zero-order hold for the input current, a discrete-time approximate recursion of SoC can be defined as:

$$SoC_k = SoC_{k-1} - \varepsilon_{eff,i}\frac{\Delta t I_{k-1}}{3600Q_n} \tag{4.8}$$

4.2 Equivalent impedance model

The observations made in the impedance measurements indicates that diffusion mechanisms operate on a much smaller time-scale than the charge-transfer kinetics. Consequently, it is often suggested that the diffusion impedance can be decoupled from the charge-transfer process [36]. In this case, the equivalent circuit in Figure 3.2 can be simplified to a modified Randles circuit shown in Figure 4.3.

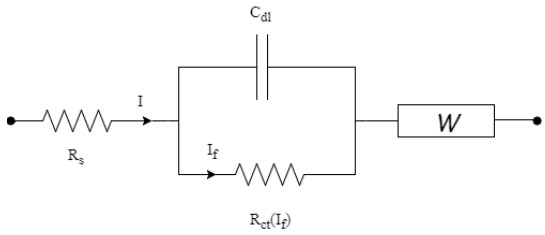

Figure 4.3: Modified Randles circuit with current dependence on the charge transfer resistance.

As observed in EIS experiments the ohmic resistance changes slowly as a function of temperature. Consequently, it is expected that an ideal series resistor can model the ohmic behavior of the cells fairly well.

[2]To get the correct scaling, the nominal capacity is multiplied with 3600 to get ampere-seconds.
[3]Note that Plett [11] use η as symbol for Coulombic efficiency.

The EIS measurements suggested a depressed semi-circle for the charge-transfer process in parallel to the electrical double layer, in which case a constant phase element for the capacitive branch provided a better fit. However, a constant phase element exhibits a fractal behavior and requires the use of fractional calculus [41] to be implementable in the time-domain. To simplify the capacitive behavior, the electrical double layer is assumed to be given by an ideal capacitor C_{dl} as in the modified Randles Circuit. The result of imposing such an assumption has already been displayed in Figure 3.6 in Chapter 3.

The dynamic change in faradaic current can be found using Kirchoff's first and second law:

$$I = I_f + I_c \qquad \eta = I_f R_{ct}(I_f) \tag{4.9}$$

where I_c is the capacitive charging current. With $I_c = C_{dl}\frac{d\eta}{dt}$, the dynamic change in faradaic current can be expressed as:

$$\frac{dI_f}{dt}(t) = -\frac{1}{R_{ct}(I_f(t))C_{dl}} I_f(t) + \frac{1}{R_{ct}(I_f(t))C_{dl}} I(t) \tag{4.10}$$

Assuming a suitably small time step Δt and zero-order hold for the instantaneous cell current $I(t)$, exact discretization yields:

$$I_{f,k} = e^{-\frac{\Delta t}{R_{ct}(I_{f,k-1})C_{dl}}} I_{f,k-1} + (1 - e^{-\frac{\Delta t}{R_{ct}(I_{f,k-1})C_{dl}}}) I_{k-1} \tag{4.11}$$

4.2.1 Including the faradaic current dependence on the charge-transfer resistance

Waag *et. al* [30] was the first to propose a battery impedance model that included the current dependency on the charge transfer process. Experimental investigations conducted by Waag *et. al* [31] show that the non-linear dependency on the current is prominent at low temperatures and as aging progresses. In continuing research conducted by Fleisher and co-authors [36, 37], the effect of the non-linear charge-transfer resistance behavior on predictability of available power for new and aged cells were considered. By imposing certain assumptions on the kinetics, it is possible to solve the Butler-Volmer Equation 2.5 explicitly. The following assumption is made with regards to the kinetics,

Assumption 1 *The anodic and cathodic reactions are assumed to be symmetric.*

which implicates $\alpha = \alpha_c = \alpha_a = 0.5$ to satisfy the requirement of $\alpha_c + \alpha_a = 1$. The other assumptions on the reaction coefficients suggested in [37], are not considered here. By employing Assumption 1, Fleischer *et. al* [37] make the following substitutions: $K = \frac{\alpha F}{R_g T}$ and $k_I = (2Ai_0)^{-1}$. The Butler-Volmer Equation 2.5 can then be expressed as:

$$I_f = \frac{1}{k_I} \frac{(e^{K\eta} - e^{-K\eta})}{2} \tag{4.12}$$

The activation overvoltage η can be expressed explicitly by the use of the hyperbolic sine function $y = sinh(x) = (e^{(x)} - e^{(-x)})/2$ and its inverse $x = sinh^{-1}(y)$, such that:

$$\eta = \frac{1}{K} sinh^{-1}(I_f k_I) \tag{4.13}$$

$$\eta = \frac{1}{K} ln\Big(I_f k_I + \sqrt{(I_f k_I)^2 + 1}\Big) \tag{4.14}$$

where the inverse hyperbolic sine function has been replaced with a logarithm according to $sinh^{-1}(x) = ln(x + \sqrt{x^2 + 1})$. Using Equation 2.6, the charge-transfer resistance can now be expressed as:

$$R_{ct}(I_f) = \frac{\eta}{I_f} \tag{4.15}$$

$$R_{ct}(I_f) = \frac{1}{K} \frac{ln\Big(I_f k_I + \sqrt{(I_f k_I)^2 + 1}\Big)}{I_f} \tag{4.16}$$

$$R_{ct}(I_f) = R_{ct,0} \frac{ln\Big(I_f k_I + \sqrt{(I_f k_I)^2 + 1}\Big)}{I_f k_I} \tag{4.17}$$

where $R_{ct,0} = \frac{k_I}{K}$ concludes the derivation made by Fleischer *et. al* [37]. Equation 4.17 contains two parameters, $R_{ct,0}$ and k_I, which defines the behavior of the non-linear charge-transfer resistance $R_{ct}(I_f)$. These parameters must be adapted on-line to account for the activation overvoltages caused by the charge-transfer process.

To the knowledge of the author of this thesis, Equation 4.17 does not directly account for the correlation between the exchange current $I_0 = Ai_0$ and the charge-transfer resistance $R_{ct,0}$ at small activation overvoltages (see Equation 3.9). Hence, in order to avoid loosing the correlation between the exchange current I_0 and the

small signal charge-transfer resistance $R_{ct,0}$, Equation 4.17 is slightly altered to be more consistent with Equation 3.9 in Chapter 3. Inserting $K = \frac{\alpha F}{R_g T}$ and $k_I = (2I_0)^{-1}$, Equation 4.17 yields:

$$R_{ct}(I_f) = \frac{R_g T}{2I_0 \alpha F} \frac{ln\Big(\frac{I_f}{2I_0} + \sqrt{(\frac{I_f}{2I_0})^2 + 1}\Big)}{\frac{I_f}{2I_0}} \tag{4.18}$$

$$R_{ct}(I_f) = \frac{R_g T}{I_0 F} \frac{ln\Big(\frac{I_f}{2I_0} + \sqrt{(\frac{I_f}{2I_0})^2 + 1}\Big)}{\frac{I_f}{2I_0}} \tag{4.19}$$

where $\alpha = 0.5$ has been inserted in the last equality. Equation 4.19 requires only I_0 to be adapted online, but requires a third assumption to be imposed:

Assumption 2 *Cell surface temperature measurements are assumed representative of the temperature in the cell as a whole, such that the absolute temperature can be expressed as* $T = 273.15 + T_{cell}$.

By Assumption 2, the correlation between the I_0 and the small signal charge-transfer resistance $R_{ct,0}$ is not lost, and the number of model parameters is reduced to tracking I_0 instead of $R_{ct,0}$ and k_I. Although Equations 4.17 and 4.19 incorporates the non-linear dependency on the faradaic current, a singularity exist at $I_f = 0$. This can result in numeric instability if not managed properly. By Using L'Hopitals rule, the limit of Equation 4.19 as $I_f \to 0$ is given by:

$$\lim_{I_f \to 0} R_{ct}(I_f) = \frac{R_g T}{I_0 F} = R_{ct,0} \tag{4.20}$$

$R_{ct}(I_f)$ must then be computed using Equation 4.19 and limit 4.20 in an if-else statement to avoid singularity issues. The remaining question now becomes how to determine when the charge-transfer process behaves sufficiently linear in order to execute the limit 4.20. Search in the literature revealed no opinion on this matter. The author of this thesis propose that the charge transfer resistance behave sufficiently like a linear resistor if $|\eta F| \ll R_g T$. Moreover, the inequality can be altered to the following form assuming sufficiently small overpotentials:

$$|R_{ct,0} I_f| \ll \frac{R_g T}{F} \tag{4.21}$$

$$|I_f| \ll \frac{R_g T}{R_{ct,0} F} = I_0 \tag{4.22}$$

$$|I_f| < \frac{I_0}{I_{limit}} \tag{4.23}$$

where the tuning parameter I_{limit} has been introduced in the last inequality. The benefit of such an approach is argued to give the system designer the possibility to consider numerical issues that may arise from computing $\frac{I_f}{2I_0}$ by tuning I_{limit}. Moreover, using inequality 4.23 enables a dynamic bound since I_0 changes as a function of cell SoC, temperature and age. The dynamic change in faradaic current in Equation 4.11 can now include the non-linear charge-transfer resistance at discrete-time invervals using the proposed procedure:

$$R_{ct}(I_{f,k}) = \begin{cases} \frac{R_g T}{I_0 F} & , |I_{f,k}| < \frac{I_0}{I_{limit}} \\ \\ \frac{R_g T}{I_0 F} \frac{ln\left(\frac{I_{f,k}}{2I_0} + \sqrt{(\frac{I_{f,k}}{2I_0})^2 + 1}\right)}{\frac{I_{f,k}}{2I_0}} & , \text{otherwise} \end{cases} \tag{4.24}$$

with $T = (273.15 + T_{cell,k})$.

4.2.2 Modeling diffusion

The diffusion phenomenon remains the most difficult process to be modelled. Kuhn *et. al* [16], and Mauracher and Karden [3], have proposed modeling the transmissive Warburg impedance (see Figure 3.3b) using an RC-network structure. The approximation of the transmissive Warburg impedance involves using Mittag-Leffler's theorem [16] and results in a structure called the Foster circuit (see Figure 4.4). For brevity, the derivation is not given here, but the reader is encouraged to read References [16, 3]. It is shown that:

$$Z_W(s) = \frac{k_2}{\sqrt{s}} tanh(\frac{k1}{k2}\sqrt{s}) \tag{4.25}$$

$$Z_W(s) = \sum_{n=1}^{\infty} \frac{R_n}{R_n C_n s + 1} \tag{4.26}$$

where,

$$R_n = \frac{8k_1}{(2n-1)^2\pi^2} \qquad C_n = \frac{k_1}{2k_2^2} \tag{4.27}$$

The diffusion phenomenon corresponding to a transmissive Warburg impedance can thus be described by a minimum set of model parameters, k_1 and k_2.

However, for an exact representation of the transmissive Warburg impedance, an unlimited amount of RC-blocks is required. Consequently, the circuit needs to be truncated by a limited amount of RC-blocks to be tractable for implementation in a real-time environment.

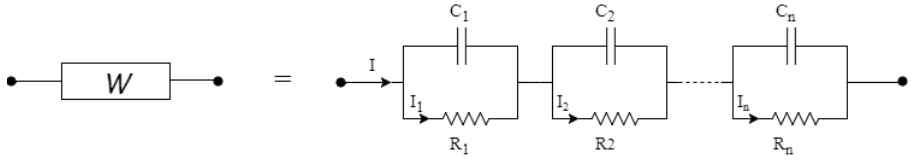

Figure 4.4: Foster structure for diffusion phenomenon corresponding to a transmissive Warburg impedance.

Using the Foster structure, a dynamic time-domain model is given by:

$$\frac{dI_n}{dt}(t) = -\frac{1}{R_n C_n} I_n(t) + \frac{1}{R_n C_n} I(t) \tag{4.28}$$

where I_n is the current passing through the n^{th} diffusion resistor. Moreover, the n^{th} diffusion over-potential is given by $V_n = R_n I_n$. Assuming a suitably small time step Δt and zero-order hold for the instantaneous cell current $I(t)$, exact discretization yields:

$$I_{n,k} = e^{-\frac{\Delta t}{R_n C_n}} I_{n,k-1} + (1 - e^{-\frac{\Delta t}{R_n C_n}}) I_{k-1} \tag{4.29}$$

The Foster circuit was originally proposed for Ni-mH [16] and lead-acid batteries [3]. Whether or not there exist any rational basis for assuming that the transmissive Warburg impedance is representative for lithium-ion batteries, the Foster circuit has been applied to lithium-ion batteries in References [37, 39].

4.3 The complete cell model

The structure of the complete cell model, used in the present work, is shown in Figure 4.5.

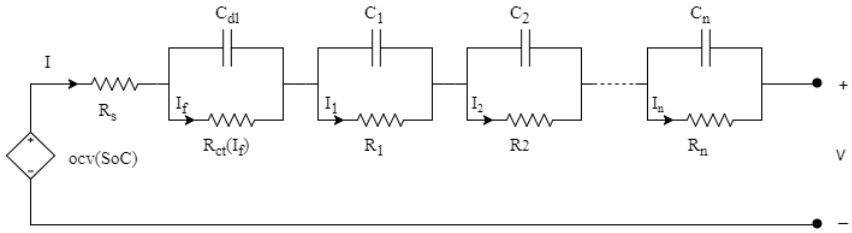

Figure 4.5: The complete cell model

The equivalent circuit model accounts for steady-state OCV-SoC dependence, and dynamic overvoltages caused by battery impedance. In summary, the battery impedance model accounts, in a phenomenological sense, for the ohmic resistance, the non-linear charge-transfer process in parallel to the electric double layer, and finally the diffusion phenomena by a modular impedance structure. The ouput voltage of the circuit can be calculated at discrete time-intervals as:

$$V_k = ocv(SoC_k) - R_s I_k - R_{ct}(I_{f,k}) I_{f,k} - \sum_{n=1}^{N} R_n I_{n,k} \tag{4.30}$$

Chapter 5

Kalman filtering

"All systems operate in the real world and therefore have to deal with uncertainty"

– Rudolph van der Merwe

Given noisy or incomplete observations, how does the BMS determine the present battery characteristics? Moreover, once an "optimal" estimate is calculated, what is the acceptable uncertainty of the inferred characteristics?

The problem of dealing with hidden variables of a system in an optimal and consistent manner given noisy or incomplete observations, is termed Probabilistic Inference, or optimal estimation theory, [13]. The incentives for employing optimal estimation theory, is that the dynamic system equations describing the cell behavior are approximations to what is actually observed. Hence, relying only on a deterministic model may lead to an inaccurate description of how the internal states, such as battery impedance characteristics and SoC, evolve in time.

The present work aims to tackle these problems by using Kalman filtering, which comprise a set of recursive equations that are repeatedly evaluated as the system operates. The central idea of Kalman filtering, is a matter of separating desired quantities, such as SoC and impedance characteristics, from a combination of signal and noise. This requires the cell model to be fit to a specific stochastic framework, given by the following generalized set of nonlinear equations:

$$\boldsymbol{\theta}_k = \boldsymbol{\theta}_{k-1} + \mathbf{e}_{k-1} \tag{5.1}$$

$$\mathbf{x}_k = \mathbf{f}(\mathbf{x}_{k-1}, \mathbf{u}_{k-1}, \boldsymbol{\theta}_{k-1}, \mathbf{w}_{k-1}) \tag{5.2}$$

$$\mathbf{y}_k = \mathbf{h}(\mathbf{x}_k, \mathbf{u}_k, \boldsymbol{\theta}_k, \mathbf{v}_k) \tag{5.3}$$

where the subscript k indicates the k^{th} sampling interval. The vector-valued process function $\mathbf{f}(\cdot)$ describes how the random state-vector $\mathbf{x}$ evolves in discrete-time intervals, while $\mathbf{h}(\cdot)$ models the existing set of states $\mathbf{x}$ and parameters $\boldsymbol{\theta}$ to a set of observations $\mathbf{y}$ that are measureable within the considered system. Both functions include the exogenous input-vector $\mathbf{u}$, and are parameterized by a parameter-vector $\boldsymbol{\theta}$. Equation 5.1 simply states that the parameters are constants, but that they may change slowly over time due to a fictitious additive noise $\mathbf{e}_{k-1}$. The stochastic process noise $\mathbf{w}$ affects the dynamic transformation of the states due to some non-measureable or non-modeled phenomenon, and $\mathbf{v}$ is the stochastic measurement noise which corrupts the observations. For generality, $\mathbf{w}$ and $\mathbf{v}$ is not assumed to affect the system additively.

The objective employing the aforementioned set of non-linear equations is to estimate SoC and adapt the impedance parameters to a particular working condition which describes the present characteristics of the cell under consideration. To estimate these quantities in an optimal[1], consistent and recursive manner however, requires that the complete description of the state and parameter probability distributions are preserved during the nonlinear transformation. Unfortunately, for non-linear systems, this may potentially require an unbounded number of statistical moments [13].

In the subsequent sections, the general framework Kalman filtering and joint-estimation is introduced. Then, the concept of the Unscented Transform, which constitutes a method for calculating the first and second-order moments of a random variable, is elaborated on. At the end of this chapter, the cell model and the joint Unscented Kalman Filter is united to form the working method on which battery states and parameters can be simultaneously estimated from only the observed noisy cell terminal voltage signal.

[1]The optimality condition used in the present work is defined as minimum mean-square error.

5.1 The Gaussian approximation

In the Kalman filter framework, all pertinent random variables are approximated by a Gaussian probability distribution:

$$p(\mathbf{x}) \sim \mathcal{N}(\hat{\mathbf{x}}, \mathbf{P}_{\mathbf{x}}) \qquad p(\boldsymbol{\theta}) \sim \mathcal{N}(\hat{\boldsymbol{\theta}}, \mathbf{P}_{\boldsymbol{\theta}}) \qquad p(\mathbf{y}) \sim \mathcal{N}(\hat{\mathbf{y}}, \mathbf{P}_{\mathbf{y}}) \tag{5.4}$$

$$p(\mathbf{w}) \sim \mathcal{N}(\mathbf{0}, \mathbf{Q}_{\mathbf{x}}) \qquad p(\mathbf{e}) \sim \mathcal{N}(\mathbf{0}, \mathbf{Q}_{\boldsymbol{\theta}}) \qquad p(\mathbf{v}) \sim \mathcal{N}(\mathbf{0}, \mathbf{R}) \tag{5.5}$$

where the state and parameter process noise, $\mathbf{w}_k$ and $\mathbf{e}_k$, and the measurement noise $\mathbf{v}_k$, are assumed to be mutually uncorrelated zero-mean Gaussian white sequences [23]. Due to the Gaussian approximation, the Kalman filter need only maintain the first and second-order moments (mean and variance) of the random variables. The rational basis for doing so, is to enable a computationally tractable solution for which the battery states and parameters can be estimated recursively in real-time.

5.2 Joint Kalman filtering

By reshaping the states and parameters to form a concatenated higher-dimensional state vector, given by $\bar{\mathbf{x}}_k = [\mathbf{x}_k^T, \boldsymbol{\theta}_k^T]^T$, the dynamic state-space equations can be expressed in the following form:

$$\bar{\mathbf{x}}_k = \bar{\mathbf{f}}(\bar{\mathbf{x}}_{k-1}, \mathbf{u}_{k-1}, \bar{\mathbf{w}}_{k-1}) \tag{5.6}$$

$$\bar{\mathbf{y}}_k = \bar{\mathbf{h}}(\bar{\mathbf{x}}_k, \mathbf{u}_k, \mathbf{v}_k) \tag{5.7}$$

where $\bar{\mathbf{w}}_k = [\mathbf{w}_k^T, \mathbf{e}_k^T]^T$, and the first and second-order moments of the joint state is given by:

$$\hat{\bar{\mathbf{x}}}_k = \begin{bmatrix} \hat{\mathbf{x}}_k \\ \hat{\boldsymbol{\theta}}_k \end{bmatrix} \qquad \mathbf{P}_{\bar{\mathbf{x}}_k} = \begin{bmatrix} \mathbf{P}_{\mathbf{x}_k} & \mathbf{P}_{\mathbf{x}_k\boldsymbol{\theta}_k} \\ \mathbf{P}_{\boldsymbol{\theta}_k\mathbf{x}_k} & \mathbf{P}_{\boldsymbol{\theta}_k} \end{bmatrix} \tag{5.8}$$

The initial format of the dynamic-state space Equations 5.1-5.3 can be recognized by the following expanded form,

$$\begin{bmatrix} \mathbf{x}_k \\ \boldsymbol{\theta}_k \end{bmatrix} = \begin{bmatrix} \mathbf{f}(\mathbf{x}_{k-1}, \mathbf{u}_{k-1}, \boldsymbol{\theta}_{k-1}, \mathbf{w}_{k-1}) \\ \boldsymbol{\theta}_{k-1} \end{bmatrix} + \begin{bmatrix} \mathbf{0} \\ \mathbf{e}_{k-1} \end{bmatrix} \tag{5.9}$$

$$\bar{\mathbf{y}}_k = \mathbf{y}_k = \mathbf{h}(\mathbf{x}_k, \mathbf{u}_k, \boldsymbol{\theta}_k, \mathbf{v}_k) \tag{5.10}$$

The central problem is a matter of propagating the joint Gaussian state variable through the system dynamics (Equation 5.6) and the observation model (Equation 5.7), by computing the statistical mean and covariance after nonlinear transformation.

$$\hat{\bar{\mathbf{x}}}_k^- = \mathbb{E}[\bar{\mathbf{x}}_k] = \mathbb{E}[\,\bar{\mathbf{f}}(\bar{\mathbf{x}}_{k-1}, \mathbf{u}_{k-1}, \bar{\mathbf{w}}_{k-1})\,] \tag{5.11}$$

$$\hat{\mathbf{y}}_k^- = \mathbb{E}[\mathbf{y}_k] = \mathbb{E}[\,\bar{\mathbf{h}}(\bar{\mathbf{x}}_k, \mathbf{u}_k, \mathbf{v}_k)\,] \tag{5.12}$$

$$\mathbf{P}_{\bar{\mathbf{x}}_k}^- = \mathbb{E}[\,(\mathbf{x}_k - \hat{\bar{\mathbf{x}}}_k^-)(\mathbf{x}_k - \hat{\bar{\mathbf{x}}}_k^-)^T\,] \tag{5.13}$$

$$\mathbf{P}_{\mathbf{y}_k} = \mathbb{E}[\,(\mathbf{y}_k - \hat{\mathbf{y}}_k)(\mathbf{y}_k - \hat{\mathbf{y}}_k)^T\,] \tag{5.14}$$

$$\mathbf{P}_{\bar{\mathbf{x}}_k \mathbf{y}_k} = \mathbb{E}[\,(\mathbf{x}_k - \hat{\bar{\mathbf{x}}}_k^-)(\mathbf{y}_k - \hat{\mathbf{y}}_k)^T\,] \tag{5.15}$$

where the superminus is a reminder that $\hat{\bar{\mathbf{x}}}_k^-$ and $\mathbf{P}_{\bar{\mathbf{x}}_k}^-$ is an *a priori* prediction-estimate of the joint state probability distribution. Using a linear combination of the noisy measurements and the prior estimates, the posterior joint state probability distribution is updated by a blending matrix $\mathbf{K}_k$ (Kalman gain), which minimizes the variance along the major diagonal of the posterior error covariance matrix $\mathbf{P}_{\bar{\mathbf{x}}_k}$:

$$\mathbf{K}_k = \mathbf{P}_{\bar{\mathbf{x}}_k \mathbf{y}_k} \mathbf{P}_{\mathbf{y}_k}^{-1} \tag{5.16}$$

$$\hat{\bar{\mathbf{x}}}_k = \hat{\bar{\mathbf{x}}}_k^- + \mathbf{K}_k(\mathbf{y}_k - \hat{\mathbf{y}}_k^-) \tag{5.17}$$

$$\mathbf{P}_{\bar{\mathbf{x}}_k} = \mathbf{P}_{\bar{\mathbf{x}}_k}^- - \mathbf{K}_k \mathbf{P}_{y_k} \mathbf{K}_k^T \tag{5.18}$$

The result of the prediction-update procedure is an estimate of the posterior joint state probability distribution that is recursively conditioned, in a statistical sense, on the entire past measurement stream [23]. For this to work. the Kalman filter requires the knowledge of the covariance of the noise sources, and an initial estimate ($\hat{\bar{\mathbf{x}}}_0$ and $\mathbf{P}_{\bar{\mathbf{x}}_0}$) that is based on all the available knowledge of the process prior to any measurement.

Further approximation must be made in terms of how the Equations 5.11-5.15 are computed due to the nonlinear nature of the considered system. The approximate solutions to nonlinear Kalman filtering, such as the Extended Kalman Filter[2] and the Unscented Kalman Filter, differ only in how the probability densities are propagated through the nonlinear functions 5.6 and 5.7, and maintained in Equations 5.11-5.18. Hence, the rationale for selecting an appropriate state and parameter estimator is rooted in their abilities to maintain the posterior mean and covariance of the joint state.

5.3 The unscented transform

The Unscented Kalman Filter (UKF) proposed by Julier and Uhlmann [4], is part of the more general Sigma-Point Kalman Filter framework [13], which relies on the principal that it is easier to approximate the probability distribution of a random variable rather than an arbitrary nonlinear function. Contrary to the analytical linearization technique employed by the Extended Kalman Filter, the UKF deterministically selects a minimum set of sigma-points whose sample mean and sample covariance has the same first and second-order moments as the current best estimate. The constructed set of sigma-points are then propagated through the nonlinear system functions to produce a new set of transformed sigma-points. The first and second order moments of the transformed set of sigma-points are then calculated using the Unscented Transform (see Equation 5.21 and 5.22).

[2]Which has been used in previously related work on battery state estimation [48, 49].

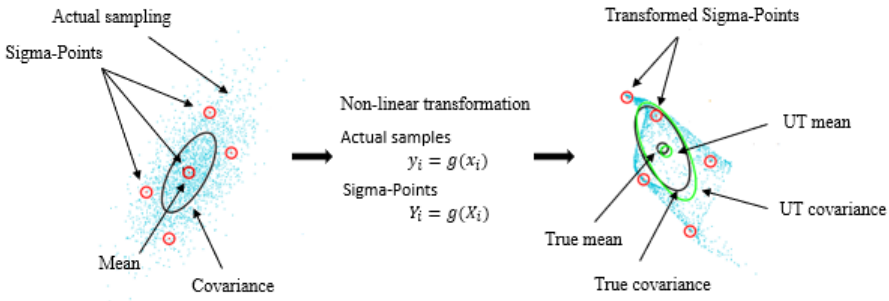

Figure 5.1: Illustration of the Unscented Transform concept. The sigma-points are propagated through an arbitrary non-linear function $g(x)$, and the mean and covariance are calculated using the Unscented Transfrom (UT). The Figure is modified into a compact form from Reference [13].

Using an arbitrary example as in Figure 5.1 with $dim(\mathbf{x}) = L$, then $2L + 1$ sigma-points are sampled according to Equation 5.19:

$$\mathcal{X} = \begin{bmatrix} \hat{\mathbf{x}} & \hat{\mathbf{x}} + \gamma\sqrt{\mathbf{P}_x} & \hat{\mathbf{x}} - \gamma\sqrt{\mathbf{P}_x} \end{bmatrix} \tag{5.19}$$

where $\mathcal{X}$ is a $L \times (2L + 1)$ sigma-point matrix, and γ is a scaling parameter. The matrix square-root $\sqrt{\mathbf{P}_x}$ is often calculated using the numerically efficient and stable Cholesky decomposition [1]. The sampled sigma-vectors $\mathcal{X}_i$ are then propagated through the nonlinear mapping function $g(\mathbf{x}) : L \rightarrow M$,

$$Transformation: \qquad \mathcal{Y}_i = g(\mathcal{X}_i) \qquad i = 0, ..., 2L \tag{5.20}$$

and the mean and covariance of the transformed set of sigma-points are calculated using a weighted sampled mean and covariance:

$$Mean: \qquad \hat{\mathbf{y}} = \sum_{i=0}^{2L} \omega_i^m \mathcal{Y}_i \tag{5.21}$$

$$Covariance: \qquad \mathbf{P}_y = \sum_{i=0}^{2L} \omega_i^{(c)} (\mathcal{Y}_i - \hat{\mathbf{y}})(\mathcal{Y}_i - \hat{\mathbf{y}})^T \tag{5.22}$$

where $\boldsymbol{\omega}^{(m)}$ and $\boldsymbol{\omega}^{(c)}$ are the weight-vectors. Moreover, γ and the weights $\omega_i^{(m)}$ and $\omega_i^{(c)}$ are selected according to a particular sampling scheme in order to capture certain information about the probability density after transformation. The sampling scheme presented here is based on the *Scaled Unscented Transform* [9, 13]. However, several other techniques for creating the weights and how sigma-points are sampled have been proposed by Julier and co-authors [2, 8, 10].

Initialization of scaled sigma-point weights:

$$\lambda = \alpha^2(L + \kappa) - L \tag{5.23}$$

$$\gamma = \sqrt{L + \lambda} \tag{5.24}$$

$$\omega_0^{(m)} = \frac{\lambda}{L + \lambda}, \qquad i = 0 \tag{5.25}$$

$$\omega_0^{(c)} = \frac{\lambda}{L + \lambda} + (1 - \alpha^2 + \beta), \qquad i = 0 \tag{5.26}$$

$$\omega_i^{(m)} = \omega_i^{(c)} = \frac{1}{2(L + \lambda)}, \qquad i = 1, ..., 2L \tag{5.27}$$

where α controls the spread of the sigma-points, β is a correction factor for the zeroth covariance weight, and κ is an additional scaling parameter. Collectively, α, β and κ are tuning parameters that determines the "characteristics" of the Kalman filter in terms of how sigma-points are sampled, and how the mean and covariance are computed using the weight-vectors $\boldsymbol{\omega}^{(m)}$ and $\boldsymbol{\omega}^{(c)}$.

5.4 Kalman filter design considering the complete cell model

In general, the state-variable comprise the unknown quantities of the battery that change on a relatively rapid time-scale in comparison to the model parameters. In the present work, the state-variable $\mathbf{x}$ includes SoC, the faradaic current and diffusion currents, while $\boldsymbol{\theta}$ comprise the set of unknown impedance parameters. Hence, the necessary assumption imposed on the impedance parameters in the present work is given by,

Assumption 3 *Impedance parameters are assumed to be changing slowly such that* $\boldsymbol{\theta} = [R_s, I_0, C_{dl}, k_1, k_2]^T$ *can be modelled as a stationary process driven by artificial zero-mean Gaussian noise* $\boldsymbol{e}$ *with covariance* $\boldsymbol{Q_\theta}$.

Rationale for selection of decision variables:

Considering the proposed modification of the charge-transfer resistance model, no prior information is given for the optimal value of I_{limit}. The value utilized in the present work is $I_{limit} = 10$. The number of RC-blocks to describe the diffusion phenomenon however, can be selected on the basis of computational requirements in the actual hardware or on the need for model fidelity. To accommodate the need for reducing the computational effort, the number of RC-blocks is limited to $N = 2$, where R_n and C_n in Equation 4.27 are computed as:

$$R_{n,k} = \frac{8k_{1,k}}{(2n-1)^2\pi^2} \qquad C_{n,k} = \frac{k_{1,k}}{2k_{2,k}^2} \tag{5.28}$$

The joint state in its expanded form, is thus given by:

$$\bar{\mathbf{x}}_k = \begin{bmatrix} \mathbf{x}_k, \boldsymbol{\theta}_k \end{bmatrix}^T \tag{5.29}$$

$$\bar{\mathbf{x}}_k = \begin{bmatrix} SoC_k, I_{f,k}, I_{1,k}, I_{2,k}, R_{s,k}, I_{0,k}, C_{dl,k}, k_{1,k}, k_{2,k} \end{bmatrix}^T \tag{5.30}$$

and readily available measurements are used as inputs and observations.

$$\mathbf{u}_k = \begin{bmatrix} I_{cell,k} \\ T_{cell,k} \end{bmatrix} \qquad y_k = V_{cell,k} \tag{5.31}$$

A second assumption is imposed on the nature of the noise sources to simplify the description of the dynamic system.

Assumption 4 *State process noise and measurement noise is assumed to affect the system additively.*

Whether or not there exist any rational basis for choosing the variance of the noise sources, the approach pursued herein has been a matter of tuning the individual variance-values off-line in order to obtain statistically satisfactory filter performance. The choice of the artificial driving noise for the impedance parameters, determines the convergence and tracking performance. However, as a note of experience, the variance-values should be carefully selected. In contrast to the state-variables SoC, I_f and I_n, the impedance parameters are only observable during dynamic excitation. That is, when the cells are in e.g. equilibrium condition, the uncertainty in the parameters will grow unbounded.

The battery management system, installed in the Revolve NTNU electric race car, samples 140 cell voltages at a rate of 10 Hz. This limits the BMS ability to observe changes in voltages between the measurements even though transients may exist. Since the sampling rate usually cannot be significantly increased in battery management systems because it could compromise other important tasks. Hence, to account for the sampling rate used in the actual vehicles, the sample-time is set to $\Delta t = 0.1$ seconds.

According to Merwe [13], $\beta = 2$ is optimal value for systems having a Gaussian distributed random variables. The parameter α was selected on the basis of Kalman filter stability, while the value of κ had little to no impact on the characteristics of the Kalman filter in the present work.

A summary of cell model and Kalman filter decision variables used in the case study (Chapter 6) can be found on the next page, and the pseudo-code in Algorithm 1 provides the necessary steps to implement the joint-UKF to estimate battery states and parameters simultaneously.

Decision variables used in the case study

Sampling time:

$$\Delta t = 0.1 \quad [s]$$

Scaled Unscented Transform parameters:

$$\alpha = 0.1$$
$$\beta = 2$$
$$\kappa = 0$$

Charge-transfer resistance linearity limit (See Equation 4.23):

$$I_{limit} = 10$$

Number of RC-diffusion blocks:

$$N = 2$$

Measurement noise variance:

$$R = 0.2^2 \quad [V]^2$$

Process noise covariance matrix:

$$\mathbf{Q_x} = \text{diag}([1e-8, 1e-4, 1e-2, 1e-2])$$
$$\mathbf{Q_\theta} = \text{diag}([1e-12, 5e-5, 5e-7, 1e-12, 1e-14])$$
$$\mathbf{Q} = \begin{bmatrix} \mathbf{Q_x} & \mathbf{0} \\ \mathbf{0} & \mathbf{Q_\theta} \end{bmatrix}$$

Algorithm 1: The Scaled Unscented Kalman Filter (UKF) - additive noise

Initialization of state mean and state covariance

$$\hat{\mathbf{x}}_0 = \mathbb{E}[\mathbf{x}_0]$$
$$\mathbf{P}_{x_0} = \mathbb{E}[(\mathbf{x}_0 - \hat{\mathbf{x}}_0)(\mathbf{x}_0 - \hat{\mathbf{x}}_0)^T]$$

Initialize sigma-point weights using Equations 5.23-5.27

for $k \in \{1, ..., \infty\}$ **do**

Calculate sigma points:

$$\mathcal{X}_{k-1} = \begin{bmatrix} \hat{\mathbf{x}}_{k-1} & \hat{\mathbf{x}}_{k-1} + \gamma\sqrt{\mathbf{P}_{x_{k-1}}} & \hat{\mathbf{x}}_{k-1} - \gamma\sqrt{\mathbf{P}_{x_{k-1}}} \end{bmatrix}$$

Time update:

$$\begin{aligned}
\mathcal{X}^*_{k|k-1} &= f(\mathcal{X}_{k-1}, \mathbf{u}_{k-1}) \\
\hat{\mathbf{x}}^-_k &= \sum_{i=0}^{2L} \omega_i^{(m)} \mathcal{X}^*_{i,k|k-1} \\
\mathbf{P}^-_{x_k} &= \sum_{i=0}^{2L} \omega_i^{(c)} (\mathcal{X}^*_{i,k|k-1} - \hat{\mathbf{x}}^-_k)(\mathcal{X}^*_{i,k|k-1} - \hat{\mathbf{x}}^-_k)^T + \mathbf{Q} \\
\mathcal{Y}_{k|k-1} &= h(\mathcal{X}^*_{k|k-1}, \mathbf{u}_{k-1}) \\
\hat{\mathbf{y}}^-_k &= \sum_{i=0}^{2L} \omega_i^{(m)} \mathcal{Y}_{i,k|k-1}
\end{aligned}$$

Measurement update:

$$\begin{aligned}
\mathbf{P}_{y_k} &= \sum_{i=0}^{2L} \omega_i^{(c)} (\mathcal{Y}_{i,k|k-1} - \hat{\mathbf{y}}^-_k)(\mathcal{Y}_{i,k|k-1} - \hat{\mathbf{y}}^-_k)^T + \mathbf{R} \\
\mathbf{P}_{x_k y_k} &= \sum_{i=0}^{2L} \omega_i^{(c)} (\mathcal{X}_{i,k|k-1} - \hat{\mathbf{x}}^-_k)(\mathcal{Y}_{i,k|k-1} - \hat{\mathbf{y}}^-_k)^T \\
\mathbf{K}_k &= \mathbf{P}_{x_k y_k} \mathbf{P}^{-1}_{y_k} \\
\hat{\mathbf{x}}_k &= \hat{\mathbf{x}}^-_k + \mathbf{K}_k(\mathbf{y}_k - \hat{\mathbf{y}}^-_k) \\
\mathbf{P}_{x_k} &= \mathbf{P}^-_{x_k} - \mathbf{K}_k \mathbf{P}_{y_k} \mathbf{K}^T_k
\end{aligned}$$

end

The pseudocode is adopted from Merwe [13].

Chapter 6

Case study - Revolve NTNU endurance run

A dynamic load profile is used as a case study with purpose to evaluate the consistency of state and parameter estimates produced by the Kalman filter during real racing conditions. The load profile depicted in Figure 6.1 has been collected from a datalogger installed in the electric vehicle "Gnist" at the Formula Student Austria 2016 Endurance event.

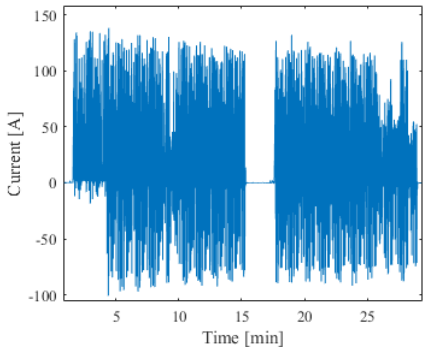

Figure 6.1: Dynamic current profile during an Endurance event at Formula Student Austria 2016. Positive and negative currents equal discharge and charge respectively. Load current is measured periodically at 3 ms time-intervals.

The Endurance event is a 22 km long racing competition, where two drivers exchange along the midpoint of the run. For the Formula Student teams partic-

ipating in the event, the scoring is based on both the energy consumption, and on how fast the electric race car finishes the entire track. Hence, the battery cells are subjected to both high-rate discharge during acceleration and high-rate charging during regenerative breaking. This particular drive-cycle is thus suitable as a case-study because it captures thermal development and the entire SoC-range of the battery cells, which subsequently affects the battery impedance characteristics. However, For this profile to be useful in a single-cell experiment in a laboratory environment, the data-set had to be preprocessed.

6.1 Preprocessing of Endurance drive-cycle data

The measured current in Figure 6.1 depicts the total current provided by a pair-wise (2p140s[1]) configuration of the Revolve battery cells. Based on the assumption that the pair-wise configured battery cells in "Gnist" had matching internal characteristics, the instantaneous load current at each sampling interval was divided by two.

Due to memory limitations in the PEC-ACT0550 battery tester, the data set had to be further simplified. First, the profile was interpolated to create a data-set with 25 ms measurement intervals. Subsequently, a 20-second long discharge sequence (Figure 6.2a) and a two-minute long high-rate discharge/charge profile (Figure 6.2b) was extracted to incorporate the dynamics of acceleration and regenerative breaking.

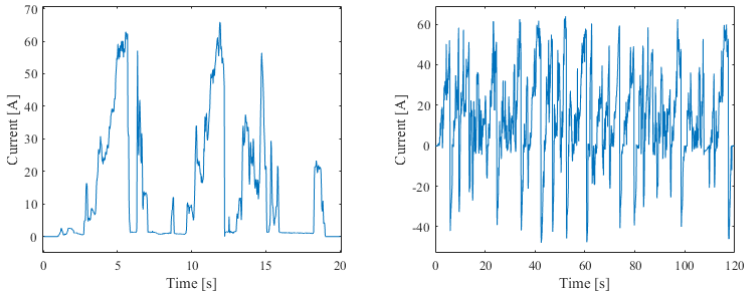

(a) Discharge (b) Discharge/charge

Figure 6.2: Extracted and preprocessed data sequences from the Endurance drive cycle in Figure 6.1.

[1] 2p = two cells connected in parallel. 140s = 140 parallel-connected cells in series.

In order to not over-charge the cells, the initial approach was to use the discharge sequence until the the cell terminal voltage was equal to 3.9 V. After this, the two-minute high-rate charge/discharge profile was initiated. This worked well for the new cell, but for the aged cell a different approach was needed due to it's higher impedance. For the aged cell, the high-rate charge/discharge currents were initiated if the cell terminal voltage at the end of the discharge-sequence was measured below 4.0 V. After running the two-minute profile consecutively seven times, a three-minute long relaxation period was used to emulate a driver exchange, after which the two-minute profile was allowed to run until the cut-off voltage of 3.0 V.

The cells were put in a Termaks thermal chamber with an ambient temperature of $25°C$. Standard four-wire configuration was used to measure cell voltage and current, in addition to applying discharge/charge currents to the specified set-point each 25 ms interval. The cell temperature was measured using a PT-100 F2020 series sensor from Omega. The test procedure was implemented using PEC's own software (LifeTest), which also monitors and records the desired information during the test.

The voltage dynamics, thermal development and calculated SoC-reference from applying the described procedure on the new and aged cell, are depicted in Figures 6.3-6.5.

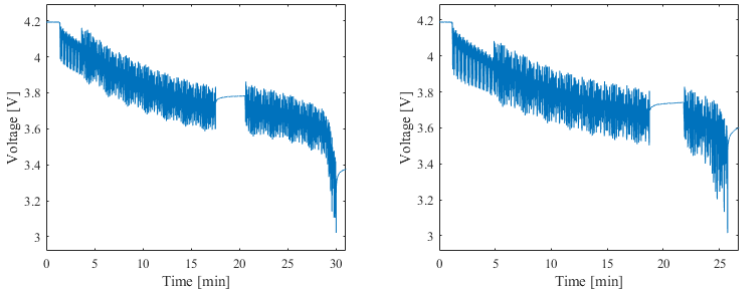

(a) New cell (b) Aged cell

Figure 6.3: Measured cell terminal voltage during the drive-cycles.

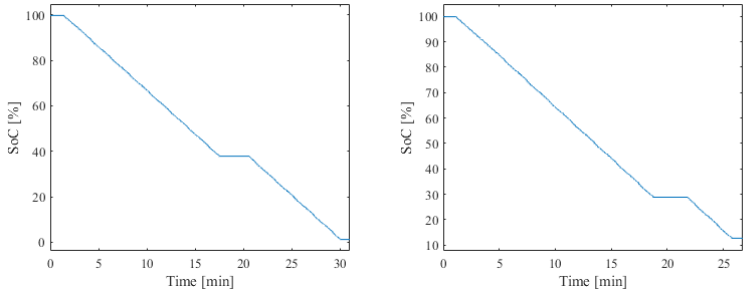

(a) New cell (b) Aged cell

Figure 6.4: SoC-reference determined by the coulomb counting method described in Chapter 4 and the ampere-hour collected data from the Drive-cycles as input.

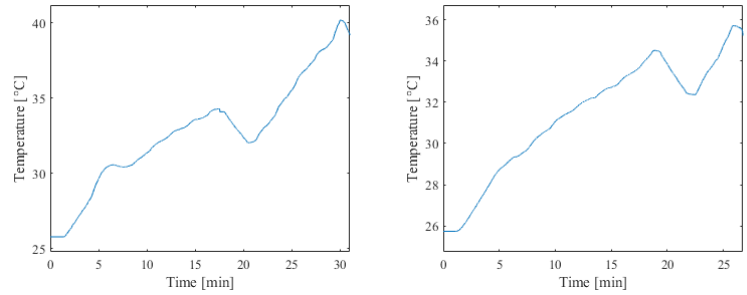

(a) New cell (b) Aged cell

Figure 6.5: Thermal developement of the new and aged cell during the drive-cycles.

6.2 Case study description

Having *a priori* knowledge of battery states and parameters may not be easily available in a given situation. Hence, the case-study aims to evaluate the Kalman filter in a condition where initial battery SoC and impedance characteristics of the respective cells are displaced from the true condition. To simplify the analysis, the Kalman filter was given equal conditions with respect to decision variables (see Chapter 5) and initial state/parameter estimates when working on the respective cells. This was done in order to simplify the analysis of the obtained data with respect to trends and consistency.

How to determine the initial conditions for the diffusion parameters was not obvious however. A practical approach was chosen, wherein the initial conditions

for the diffusion parameters were determined by a trial and error process until the diffusion parameters were close to what seems to be incorporating some, presently unknown, "truth" of the underlying cell characteristics for both the new and aged cell.

The Joint Unscented Kalman Filter, summarized in Algorithm 1 in Chapter 5, was implemented in a Matlab script.

6.3 Construction of impedance parameter reference values

The impedance characteristics for the new and aged cell during the drive cycle, were extracted using linear interpolation with temperature measurements and SoC reference as inputs to the parameter look-up tables constructed in Chapter 3. It is assumed that the generated set of reference parameters, shown in Figures 6.6-6.9, can be used for evaluating the trend and consistency in estimated impedance parameters for the respective cells.

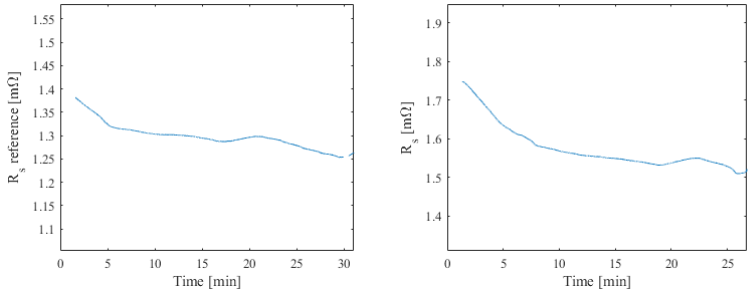

(a) New cell (b) Aged cell

Figure 6.6: Ohmic resistance R_s reference

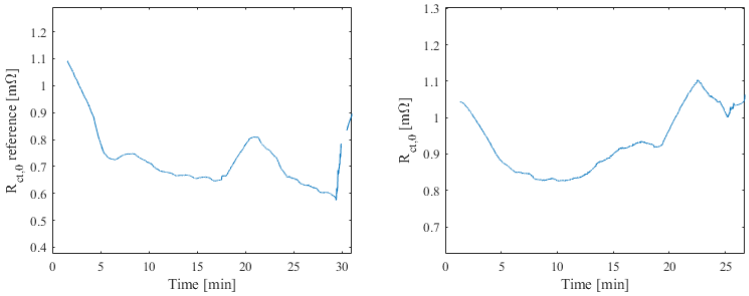

(a) New cell (b) Aged cell

Figure 6.7: Small-signal charge transfer resistance $R_{ct,0}$ reference

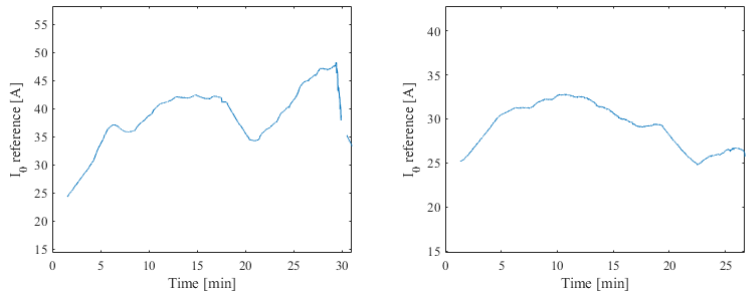

(a) New cell (b) Aged cell

Figure 6.8: Exchange current I_0 reference

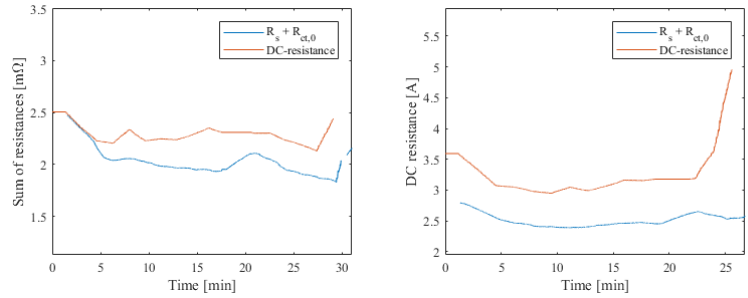

(a) New cell (b) Aged cell

Figure 6.9: Sum of resistances ($R_s + R_{ct,0}$) and DC-resistance reference

6.4 Kalman filter on a new and aged cell

The performance of the Kalman filter, working on the new and the aged cell, is demonstrated in following sub-chapters with the selected initial conditions shown below.

State and parameter initial conditions

$$\hat{\mathbf{x}}_0 = \begin{bmatrix} SoC \\ I_f \\ I_1 \\ I_2 \end{bmatrix} = \begin{bmatrix} 0.5 \\ 0 \\ 0 \\ 0 \end{bmatrix} \qquad \hat{\boldsymbol{\theta}}_0 = \begin{bmatrix} R_s \\ I_0 \\ C_{dl} \\ k_1 \\ k_2 \end{bmatrix} = \begin{bmatrix} 1.6e-3 \\ 40 \\ 50 \\ 4e-3 \\ 3e-4 \end{bmatrix}$$

$$\mathbf{P}_{\mathbf{x}_0} = \text{diag}(\,[0.2,\, 1e-8,\, 1e-5,\, 1e-5]^2\,)$$
$$\mathbf{P}_{\boldsymbol{\theta}_0} = \text{diag}(\,[0.2e-3,\, 25,\, 25,\, 1e-3,\, 1e-4]^2\,)$$

$$\bar{\mathbf{x}}_0 = \begin{bmatrix} \hat{\mathbf{x}}_0 \\ \hat{\boldsymbol{\theta}}_0 \end{bmatrix} \qquad \mathbf{P}_{\bar{\mathbf{x}}_0} = \begin{bmatrix} \mathbf{P}_{\mathbf{x}_0} & \mathbf{0} \\ \mathbf{0} & \mathbf{P}_{\boldsymbol{\theta}_0} \end{bmatrix}$$

6.4.1 Evaluation of predicted cell voltage

In Figure 6.10a, there seems to be a very close agreement between the measured and predicted cell voltages for the new cell. The aged cell also show relatively good predictions as adaption of model states and impedance parameters proceeds.

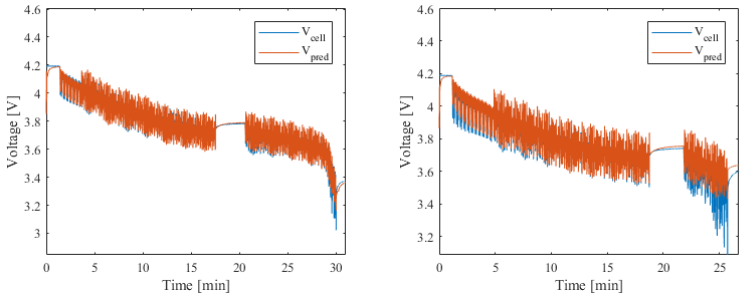

(a) New cell (b) Aged cell

Figure 6.10: Measured vs predicted cell voltage.

The largest prediction error occurs at the end-of-discharge, and during the fast transitions between discharge and charge currents. What stands out however, is the substantial estimation error for the aged cell at low SoC in Figure 6.11. This is probably related to limited diffusion to the surface of the electrodes, which is not captured with the given decision variables and the assumption that impedance parameters can be modelled as stationary signals.

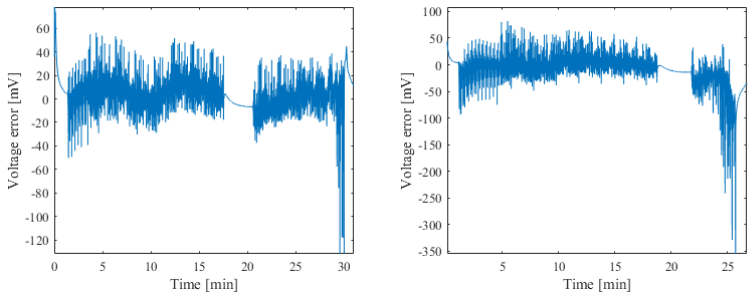

(a) New cell (b) Aged cell

Figure 6.11: Cell voltage prediction error.

Figure 6.12 depicts an empirical probability distribution of the voltage prediction error overlaid with a Gaussian fit. The constructed empirical distribution is calculated as,

$$\text{Empirical error distribution} = \frac{V_{cell} - V_{pred}}{std(V_{cell} - V_{pred})} \tag{6.1}$$

utilizing the entire measurement and prediction sequences of cell voltages as input,

and the Matlab function $std(\cdot)$.

For the new cell, the prediction error resembles a Gaussian zero-mean error distribution. For the aged cell however, the distribution is slightly biased towards the negative side, possibly, due to larger prediction errors at the start and end of the simulation.

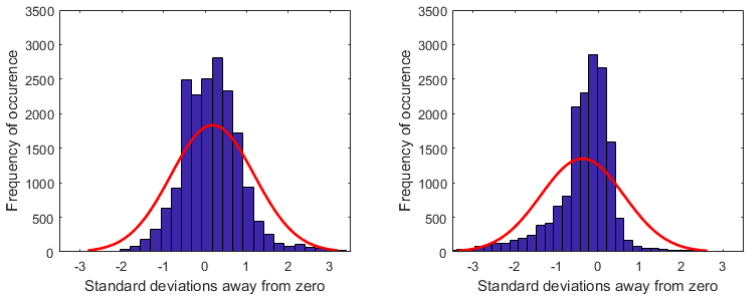

(a) New cell (b) Aged cell

Figure 6.12: Empirical probability distribution of voltage prediction error overlaid with a Gaussian fit. Matlab function $histfit(\cdot)$.

So far, only the estimation of outward appearance of the new and the aged cell have been considered. In a more thorough analysis of the underlying characteristics, however, the subsequent question is how consistent the estimated impedance parameters are compared to the reference values.

6.4.2 Evaluation of impedance parameter estimation

The constructed set of impedance reference values in Figures 6.6-6.9 are related to the fast dynamics of the cell. A closer examination of the cell dynamics and the predicted cell voltage is provided in Figure 6.13.

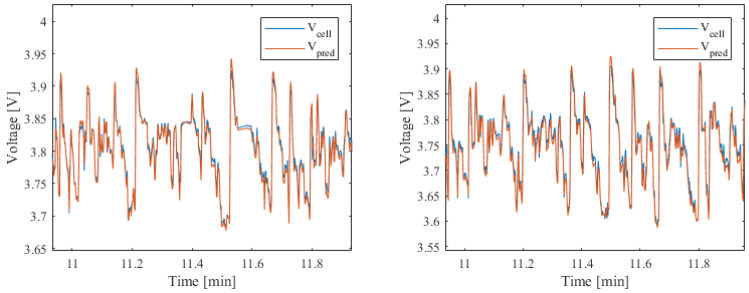

(a) New cell (b) Aged cell

Figure 6.13: Measured vs predicted cell voltage - zoomed in on fast transition dynamics.

A closer examination of the curves plotted for the new and the aged cell in Figure 6.14, reveal poor confidence, and no convergence of the expected mean of the ohmic resistances towards the "true" ohmic resistances for the respective cells. The trend, at the end-of-discharge for the aged cell, suggests that the Kalman filter corrects the series resistance in order to account for the increased voltage prediction error observed in Figure 6.11b.

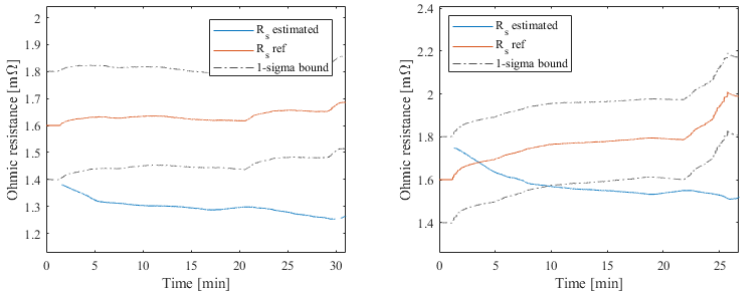

(a) New cell (b) Aged cell

Figure 6.14: Estimated Ohmic resistance vs EIS reference.

Figure 6.15 shows the estimated exchange current. For both the new and the aged cell, the initial mean-estimate of the exchange current is corrected towards the reference value. The trend, for both the new and the aged cell, shows an increase in the exchange current estimate as cell temperature increases. This is consistent with the observed dependence on cell temperature from Chapter 3. However, in similarity to the estimated ohmic resistance, the 1-sigma estimate is large.

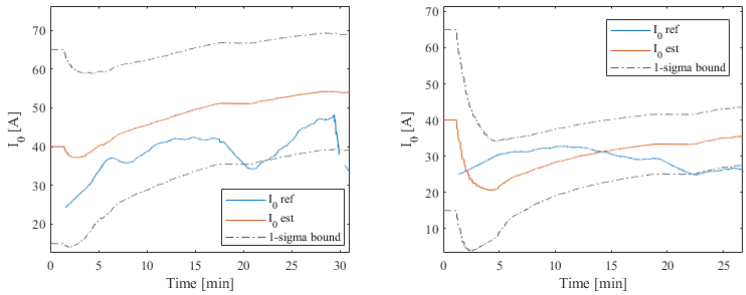

(a) New cell (b) Aged cell

Figure 6.15: Estimated exchange current vs EIS reference.

The expected mean of the small-signal charge-transfer resistance is calculated at each time-step using Equation 3.9, with the cell temperature measurements and estimated mean of the exchange current as inputs:

$$\hat{R}_{ct,0} = \frac{R_g(273.15 + T_{cell})}{\hat{I}_0 F} \tag{6.2}$$

However, due to the nonlinear nature of Equation 6.2, only a rough estimate on the 1-sigma bound can be calculated. The 1-sigma calculated herein, is based on:

$$\sigma_{R_{ct,0}} \approx \frac{R_g(273.15 + T_{cell})}{(\hat{I}_0 + \sqrt{\sigma^2_{I_0}})F} - \hat{R}_{ct,0} \tag{6.3}$$

$\sigma^2_{I_0}$ is the estimated variance extracted from the covariance matrix $P_{\bar{x}}$. The small-signal charge-transfer resistance, based on Equation 6.2 and 6.3, is shown in Figure 6.16. Clearly, the error in the estimated exchange current impacts the ability to estimate the small-signal charge-transfer resistance accurately. The behavior of the non-linear charge-transfer resistance is given in Appendix A.

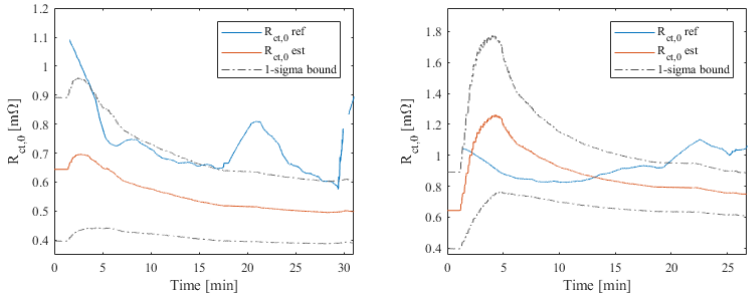

(a) New cell (b) Aged cell

Figure 6.16: Estimated charge-transfer resistance vs EIS reference.

The sum-of-resistances can be evaluated by a linear-combination of the series resistance and the small-signal charge-transfer resistance:

$$\hat{R}_{sum} = \hat{R}_s + \hat{R}_{ct,0} \tag{6.4}$$

$$\sigma_{R_{sum}} \approx \sqrt{\sigma_{R_s}^2} + \sigma_{R_{ct,0}} \tag{6.5}$$

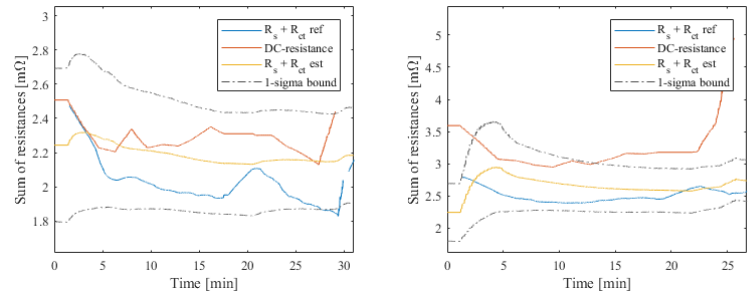

(a) New cell (b) Aged cell

Figure 6.17: Estimated sum-of-resistances ($R_s + R_{ct,0}$) vs EIS and DC-resistance reference.

Although the confidence of the expected mean of the individual circuit-elements (R_s, I_0, and $R_{ct,0}$) are poor, the expected mean of the sum-of-resistance (Figure 6.17) is in close proximity of the sum-of-resistance from EIS and DC-resistance measurements over wide range of SoC. What stands out however, is the difference between the EIS reference and the DC-resistance measurements for the aged cell

at low SoC. In this particular situation, the DC-resistance measurements are the most accurate measurements considering the large overvoltages from Figure 6.10. Hence, the error observed in the estimated sum-of-resistances for the aged cell, is most likely due to the aforementioned problem of limited diffusion and choice of Kalman filter decision variables and model assumptions.

The relatively large 1-sigma estimates for the impedance parameters are attributed to the fast electrode reaction characteristics these cells exhibits in the given range of cell temperatures they are operated in. Although not discussed up to this point, it would be logical to assume that the load-dynamics and the measurement sampling conditions plays an important role to which extent these parameters can be separated from each other during the rapid cell voltage dynamics.

As a proof of concept that the potential ambiguity in separating the processes originates from the fast electrode kinetics, the drive-cycle is repeated, but for a simpler model where the series resistance and the non-linear charge-transfer model are merged into a single series resistance (See Figure 6.18).

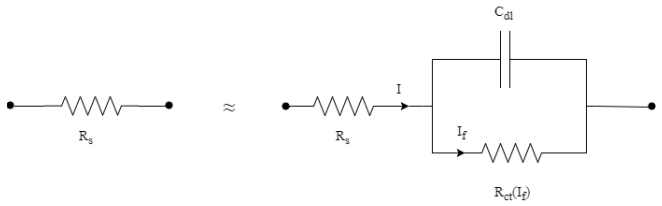

Figure 6.18: Simplified series-resistance model.

In Figure 6.19, the Kalman filter with model-reduction produces similar performance in the estimated mean of the sum-of-resistances, but with a higher confidence. Moreover, Figure 6.20 shows that the voltage prediction errors in the fast transitions between discharge and charge currents are reduced. This is due to removing the lowpass filtering behavior of the R_{ct}-C_{dl} branch.

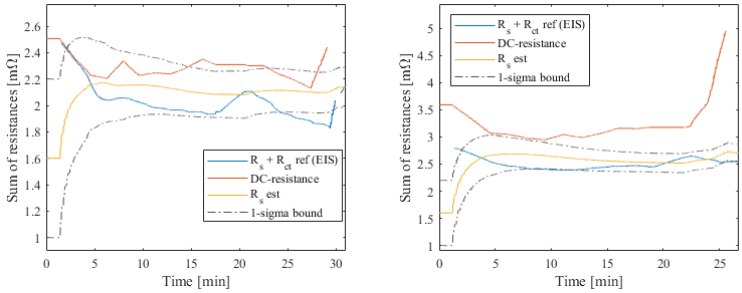

(a) New cell (b) Aged cell

Figure 6.19: Merging the series resistance and charge-transfer model into a single series resistance. Initial mean estimate $R_s = 1.6m\Omega$ and variance of $(0.6m\Omega)^2$ at time $k = 0$.

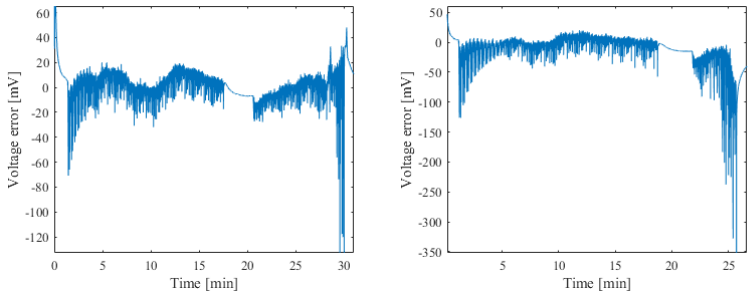

(a) New cell (b) Aged cell

Figure 6.20: Voltage prediction error when simplifying the cell model

6.4.3 Comparison of diffusion impedance between new and aged cell

The diffusion impedance is related to the slow dynamics of the cell, and is more easily observed, as a phenomenon, during relaxation when a cell is disconnected from the load. A closer examination of the slow cell dynamics and the predicted cell voltage is provided in Figure 6.21. Disregarding uncertainty considerations, this sub-chapter demonstrates differences in the behavior of the diffusion characteristics per se.

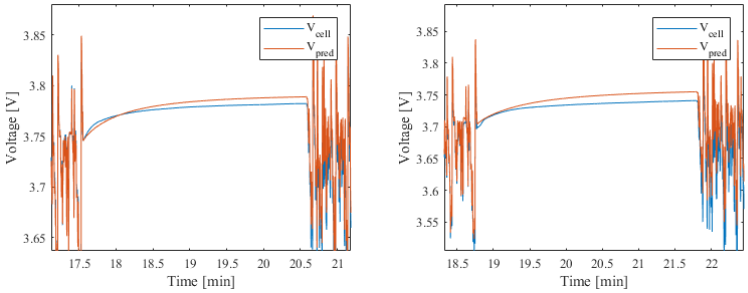

(a) New cell (b) Aged cell

Figure 6.21: Measured vs predicted cell voltage - zoomed in on diffusion during relaxation.

Figure 6.22 shows the estimated diffusion resistances, which depends on the model parameter k_1 (see Equation 4.27). The point to be made here, is that there's a distinct difference in trend given the initial conditions. That is, the aged cell showed increased diffusion resistances compared to the new cell.

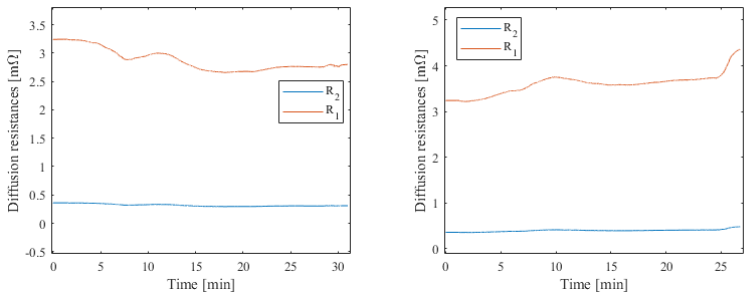

(a) New cell (b) Aged cell

Figure 6.22: Diffusion resistances.

Due to the connection between the RC-parameters, the Foster circuit models the diffusion characteristics by a dispersion of time-constants as shown in Figure 6.23.

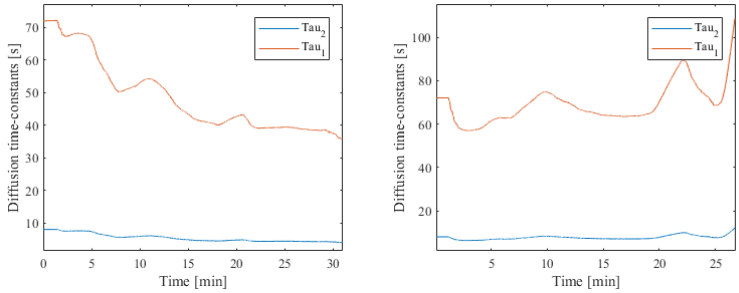

(a) New cell (b) Aged cell

Figure 6.23: Diffusion time-constants.

There are some fluctuations in the diffusion time-constants, possibly due to the reduced number of RC-blocks, which may be affected by the adaption of parameters k_1 and k_2 to correct for voltage prediction errors.

Interpreting the significance of the estimated parameters k_1 and k_2 is difficult. However, for a potential information value, the results are provided as supplementary in Appendix A. Nevertheless, the challenges of utilizing the inferred diffusion characteristics is discussed in Chapter 7.

6.4.4 Evaluation of State-of-Charge estimation

Figure 6.24 shows the estimated SoC versus SoC-reference for the new and aged cell, and Figure 6.25 shows the SoC-error and the estimated 1-sigma (68% confidence interval). For the sake of argument, an initial error of 50% is in most cases an unlikely situation. A good starting point, if no better initial expectation of SoC is available, could be based on $\mathbb{E}[SoC_0] \approx ocv^{-1}(V_0)$, assuming equilibrium conditions when the first measurement of cell voltage is available. However, validating convergence is useful for assessing correctness of the Kalman filter.

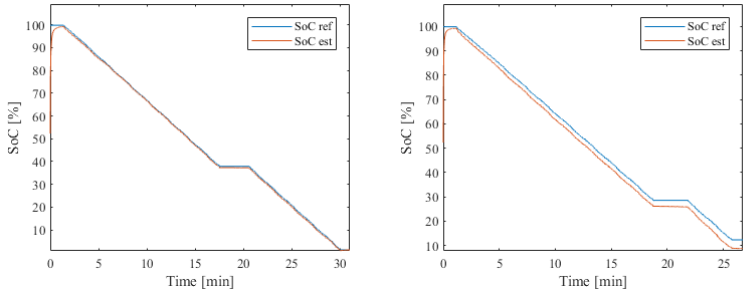

(a) New cell (b) Aged cell

Figure 6.24: SoC estimation.

The SoC-error for the new cell in Figure 6.25a suggests that the estimated SoC-mean is slightly biased, with the error below 1% after convergence. Moreover, the SoC-error is consistently within the 1-sigma bound, which in a statistical sense, suggests that the Kalman filter produces conservative estimates of the uncertainty on the estimated SoC-mean.

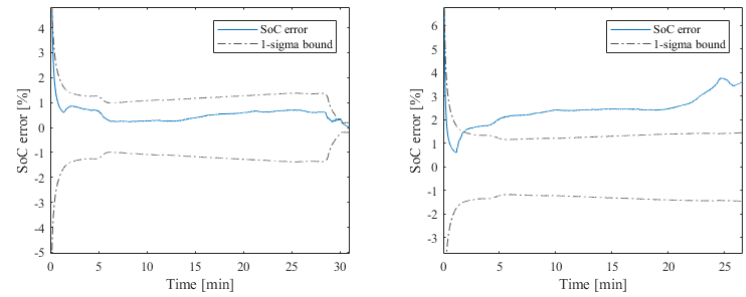

(a) New cell (b) Aged cell

Figure 6.25: SoC estimation error.

A similar manifestation can be seen for the aged cell. However, with an increased biased SoC-mean estimate, especially towards low SoC. Additionally, the SoC-error is no longer encapsulated within the 1-sigma-bound, but in general within the estimated 2-sigma (95 % confidence interval).

A closer examination of the predicted open-circuit voltage relative to the true $ocv(SoC_{true})$ and the measured terminal voltage may give useful insight as to why the SoC-estimates are biased. Note that the true open-circuit voltage and SoC_{true}, as predicted by $ocv(SoC_{true})$, also depend on the method for constructing their

mutual dependence (Chapter 4). As these cells are operated far from equilibrium conditions due to sustained passage of discharge and charge currents during the drive-cycle, the impedance model plays an important role in order to describe the displacement in cell terminal voltage from the true open-circuit voltage. In particular, the slow diffusion process may affect the SoC estimates as changes in SoC and diffusion voltages occur on similar time-scales.

The following Figures 6.26-6.28 illustrates the predicted open-circuit voltage at three different time-frames during the drive-cycle for the new and aged cell. The Figures includes the "true" and predicted open-circuit voltage, $ocv(SoC_{true})$ and $ocv(SoC_{est})$ respectively, relative to the measured cell terminal voltage.

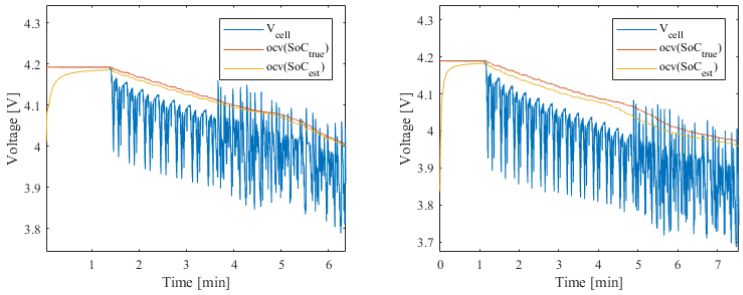

(a) New cell (b) Aged cell

Figure 6.26: Open-circuit voltage prediction at the start of the drive-cycle.

In Figure 6.26, considering both the new and aged cell, the $ocv(SoC_{est})$ converges towards the true open-circuit voltage. The constructed relationship (Chapter 4) seems to work quite well for the new cell during load, in the sense that the predicted $ocv(SoC_{est})$ is not displaced far from the presumably true open-circuit voltage $ocv(SoC_{true})$. For the aged cell however, there's a clear indication that the predicted $ocv(SoC_{est})$ is displaced from $ocv(SoC_{true})$.

Figure 6.27 shows the time-frame when the cells are disconnected from the load. During the relaxation towards equilibrium conditions, the predominant mode of cell polarization is caused by slow diffusion. Note however, that 3 minutes of relaxation is not enough to reach equilibrium conditions[2], so it can be expected that the cell terminal voltage will continue its relaxation process.

[2]From experience, these cells require about 15 minutes, or more depending on SoC and temperature, to move towards the equilibrium condition.

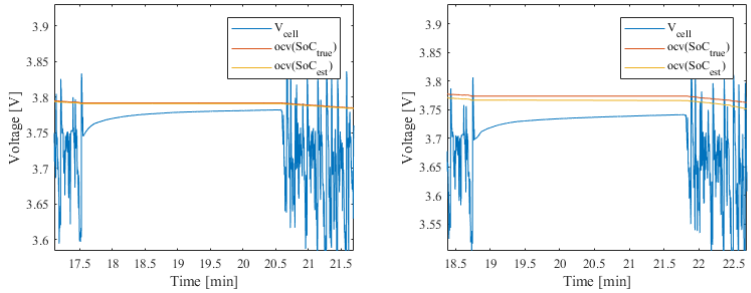

(a) New cell (b) Aged cell

Figure 6.27: Open-circuit voltage prediction during relaxation (driver exchange).

For both cells, the cell voltage seems to relax towards a different equilibrium condition compared to $ocv(SoC_{true})$ and $ocv(SoC_{est})$. This assertion is more prominent for the aged cell. The point to be made, is that the Kalman filter may adjust the level of SoC to account for errors in the innovation $V_{cell,k} - V_{pred,k}$. Most likely due to the absence of an electrochemical phenomena in the cell model influencing the equilibrium condition.

To substantiate the effect of relaxing towards different equilibrium conditions, a displacement of only ± 10 mV from $OCV(SoC_{true}) = 3.770$ V, can result in a SoC-bias of about $\pm 4\%$, which explains the error in the error in the estimated SoC-mean for the aged cell.

As SoC continues to decrease, the cell terminal voltage approaches the end-of-discharge, as shown in Figure 6.28.

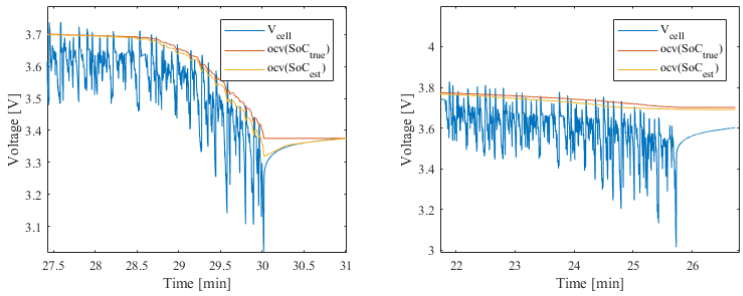

(a) New cell (b) Aged cell

Figure 6.28: Open-circuit voltage prediction towards the end-of-discharge

Here, the new cell enters the exponential decaying zone in the open-circuit

voltage, while the aged cell is increasingly polarized as previously mentioned.

Clearly, a more detailed model is required to describe the observed error in relaxation of cell terminal voltage towards equilibrium conditions for the aged cell. Thus, in the Author's opinion, the biased SoC-mean is manifested in the Kalman filter's attempt to correct for the absence of unmodelled electrochemical phenomena. One possibility is the absence of thermal dependence on the open-circuit voltage, as previously mentioned in Chapter 4. However, a second cause, is the absence of a hysteresis-model.

Electrochemical hysteresis is a phenomenon in which the cell terminal voltage relaxes to a value other than the true open-circuit voltage depending on whether the cell has been charged or discharged prior to a relaxation phase [42]. There is a distinct difference between hysteresis voltages, and overvoltages caused by slow diffusion. While diffusion-voltages slowly decay with time when the cell is allowed to rest, the hysteresis voltages persists and changes only when SoC changes.

In summary, the source of biased SoC estimates seems to be negligable for the the new cell. However, as aging proceeds, the inclusion of e.g. thermal dependence on the open-circuit voltage or a hysteresis model becomes increasingly important to reduce the bias.

Chapter 7

Addressing the challenges of on-line battery impedance and SoC estimation

Utilizing the proposed cell model and the joint Unscented Kalman Filter, several challenges were identified related to both impedance characterization and estimation of SoC at real racing conditions.

7.1 How to separate the underlying cause of error?

The point of departure for evaluating the battery impedance characteristics produced by the Kalman filter during real racing conditions, was to gather impedance measurement from two commonly used techniques - electrochemical impedance spectroscopy and DC-resistance characterization. Although EIS is useful for understanding the electrochemical mechanisms that governs the impedance response, the measurements rely on the principle of (quasi) linear-time-invariance. Thus, extracted impedance parameters describes the system response close to equilibrium conditions. Since the Revolve battery cells are usually operated quite far from equilibrium conditions, the DC-resistance measurements were useful in supporting the evaluation of the estimated impedance parameters.

The challenge of analysis is to separate the underlying cause of error, which originates from either model simplifications or Kalman filter assumptions and decision variables. Equal conditions with respect to decision variables and initial state and parameter estimates were given to simplify the analysis of estimated internal characteristics of both the new and the aged cell.

7.2 Model-reduction to better describe the battery SoH

To the outward appearance only, the voltage prediction error resembled a Gaussian zero-mean error distribution for the new cell, and less so for the aged cell. Surely, the joint Unscented Kalman filter will update the model states and parameters statistically in a minimum mean-squared error sense. However, due to the non-linear nature of the battery cells, these quantities can only be estimated sub-optimally. As shown in the case study, there is no guarantee that impedance parameters converge towards meaningful values with good confidence.

Given the imposed sampling conditions and load-dynamics, the respective impact of the ohmic resistance and the non-linear charge-transfer dynamics on the overvoltages, is difficult to separate due to the fast electrode kinetics of the cells at temperatures above $25°C$. Hence, the estimated impedance parameters describing the rapid cell dynamics are poorly conditioned on the voltage measurements, which results in non-converging expected mean of impedance characteristics with relatively high uncertainty. As a proof of concept, a simplification was introduced to verify the impact of model-reduction. The results indicated a similar estimation performance with respect to the expected mean of the sum-of-resistances, but with higher confidence in its inferred value. Thus, the concatenation of ohmic resistance and charge-transfer dynamics into a single series resistance to represent both passive and active electrochemical effects, is likely to be the best candidate to describe the battery State-of-Health in terms of its impedance characteristics in the given range of operating temperatures.

The persisting estimation error for the aged cell with respect to impedance characteristics at low SoC, is probably related to limited diffusion, which is not captured with the given Kalman filter decision variables, in addition to assumption that impedance parameters can be modeled as stationary signals. Hence, these results require more attention if reliability at low SoC must be guaranteed.

Although the significance of the estimated diffusion parameters have yet to be

discovered, a valid question would be to ask if there's a way to determine the present State-of-Health or cell performance based on diffusion characteristics. That is, can diffusion characteristics be useful to identify occurrence of deficiencies within the considered cell? In addition, how much can we trust the Kalman filter to produce representative estimates on diffusion characteristics, when the model itself is a considerable simplification of the true underlying diffusion phenomenon? Taking diffusion characteristics into consideration when discussing State-of-Health is, to the author's knowledge, scarce in literature within the field of battery monitoring.

For the new cell, the SoC estimates are consistently within the 1-sigma error bound, with a maximum estimation error of 1% after convergence. Considering the aged cell however, cell terminal voltage relaxes towards a different open-circuit voltage equilibrium state compared to the, presumably, "true" open-circuit voltage as predicted by $ocv(SoC_{true})$. The impact, is an increasingly biased SoC estimate compared to the new cell. However, the biased SoC mean is still within the 2-sigma error bound. The biased estimates were attributed to unmodelled phenomena such as missing thermal dependence on the open-circuit voltage or the absence of a model to describe the electrochemical hysteresis phenomenon.

7.3 Advantages and limitations

The motivation for modeling the faradaic current dependency on the charge-transfer resistance was based on the work by Fleisher and co-authors [36, 37]. However, the method were modified to estimate the exchange current I_0 with the assumption that cell temperature measurements are descriptive of the overall cell temperature. This was done, in order to arrive at a non-linear charge-transfer model which could be compared with results obtained by means of impedance spectroscopy. Thus, to the knowledge of the author, the validity of the proposed modification depends the assumption that cell temperature measurements can be used as input to the model and on the Kalman filter's ability to estimate the exchange current.

Even though the proposed modifications to the non-linear charge-transfer model is inconclusive in terms of its impact on battery monitoring, the model-reduction indicated that the non-linearity is negligible for the cells used in the case study at normal and elevated cell temperatures. Considering that the Revolve battery cells are rarely operated below $20°C$, the simplified model is suggested for further use.

Nevertheless, the faradaic current dependency on the charge-transfer reaction is reported [30] to be substantial at low temperatures and as battery aging progresses.

Chapter 8

Further work

Only a single drive-cycle has been pursued as a case study to evaluated the performance of the Kalman filter to estimate battery SoC and impedance characteristics. To the author's opinion, a longer time-series comprising several cycles and different driving situations would be helpful in uncovering possible weaknesses in the method investigated herein. Given a longer time-series, one could additionally evaluate the Kalman filter's ability to track ongoing degredation as the system operates, rather than evaluating its performance within a small time-frame. For instance, the evaluation over a longer time-series can be done by running characterization tests before and after several cycles for comparison with the estimated impedance parameters. Moreover, such a case study can be extended to include estimation of cell capacity, which is also of significant importance in terms of State-of-Health and its impact on SoC estimation.

Based on the SoC estimation results, the author suggests to investigate the impact of thermal dependency on the open-circuit voltage and the electrochemical hysteresis, and how it affects SoC estimation as aging proceeds.

As stated in Chapter 5, the Kalman filtering framework relies on the assumption that all pertinent random variables can be described by a Gaussian probability distribution, and that the noise affecting the process and measurement functions are white. However, to the author's knowledge, literature on the validity of the Gaussian assumption to lithium-ion cells is scarce. In particular, the validity of the assumption over the expected lifetime of the battery cells and at different cell temperature conditions would be an interesting field of research. This could be

compared to relatively new cells operated at normal temperatures, for which most of existing literature considers. Additionally, the research could also be accompanied by non-Gaussian algorithms, such as the Particle filter, to assess in what situations Kalman filtering is the most suitable estimator.

On pursuit of optimizing real-time performance of Kalman filtering for state and parameter estimation of large battery packs, the author suggests looking into "bar-delta" filtering proposed by Plett [50]. The general idea of "bar-delta" filtering is to run two separate kalman filters in parallel. The "bar"-filter is a joint Unscented Kalman Filter working on the average response of the battery pack, resulting in an average estimate on battery state and parameters. For N numbers of cells connected in series, N number of "delta" Kalman filters work on estimating the difference between battery states and parameters from the pack-average response. Since battery packs are designed using cells with similar characteristics when new, the "delta"-filter can run less frequently, and thus results in decreased computational burden to estimate SoC and battery impedance characterstics on cell level.

Moreover, the dual estimation approach can also decrease the computational burden. Plett [17, 18] show results of running both Joint and Dual estimation on a lithium-ion polymer cell, using a variety of Kalman filters such as the Unscented Kalman Filter, the Central Difference Kalman Filter, and their square-root forms. A thorough collection on Sigma-Point Kalman Filters can be found in Reference [13].

Chapter 9

Conclusion

Utilizing a dynamic drive-cycle representative of real racing conditions, the battery impedance and SoC were estimated for a new and an aged lithium-polymer battery cell. The given method used, was a joint Unscented Kalman Filter coupled with a non-linear equivalent circuit battery model. The point of departure for evaluating the battery impedance characteristics produced by the Kalman filter, was to gather impedance measurements from two commonly used techniques - electrochemical impedance spectroscopy and DC-resistance characterization. Given the imposed sampling conditions and load-dynamics, the respective impact of the ohmic resistance and the non-linear charge-transfer dynamics on the overvoltages, was difficult to separate due to the fast electrode kinetics of the cells at temperatures above $25°C$. As a result, the estimated impedance parameters describing the rapid cell dynamics were poorly conditioned on the voltage measurements. As a proof of concept, a simplification was introduced in order to verify the impact of a model-reduction. The results indicated a similar estimation performance with respect to the expected mean of the sum-of-resistances, but with a higher confidence in its inferred value. Thus, for the considered lithium-polymer battery cells operated at cell temperatures above $25°C$, the concatenation of ohmic resistance and charge-transfer dynamics into a single series resistance is likely to be the best candidate to describe the battery State-of-Health in terms of their impedance characteristics. The outcome of the simplification is reduced computational effort due to model reduction, and increased confidence in the inferred sum-of-resistance by allowing the series resistance to represent both passive and active electrochemical effects. However, the estimation error for the aged cell with respect to impedance

characteristics at low SoC, still persists. This is probably related to limited diffusion, which is not captured with the given Kalman filter decision variables, in addition to assumptions of how impedance parameters evolve in time. Moreover, secondary results showed that SoC can be estimated very accurately for the new cell, with a maximum estimation error of about 1%. However, due to non-modelled phenomena such as electrochemical hysteresis and thermal dependency on the open-circuit voltage, the SoC estimates for the aged cell was biased in the range of 2-4%. The reliability of most BMS functions depends on its ability to track the battery SoC and impedance characteristics, and more importantly, in a consistent manner over the expected battery lifetime. Thus, if high reliability in a wide range is desirable, further work should concentrate on how to reduce the estimation error with respect to impedance characteristics at low SoC, and the influence of non-modelled phenomena on the equilibrium conditions.

Bibliography

[1] W. H. Press; S. A. Teukolsky; W. T. Vetterling; and B. P. Flannery. *Numerical Recipes in C: The Art of Scientific Computing*. 2nd ed. Cambridge, U.K.: Cambridge Univ. Press, 1992.

[2] S. J. Julier; J. K. Uhlmann; H. F. Durrant-Whyte. "A New Approach for Filtering Nonlinear Systems". In: *Proc. Amer. Control Conf.* (1995), pp. 1628–1632.

[3] P. Mauracher; E. Karden. "Dynamic modelling of lead/acid batteries using impedance spectroscopy for parameter identification". In: *J. of Power Sources (67)* (1997), pp. 69–84.

[4] S. J. Julier; J. K. Uhlmann. "A New Extension of the Kalman Filter to Nonlinear Systems". In: *Proc. SPIE* 3068 (1997), pp. 182–193.

[5] E. Karden; S. Buller; R.W. De Doncker. "A method for measurement and interpretation of impedance spectra for industrial batteries". In: *J. of Power Sources (85)* (2000), pp. 72–78.

[6] S. Surampudi B.V. Ratnakumar; M.C. Smart. "Electrochemical impedance spectroscopy and its applications to lithium ion cells". In: *17-th Annual Battery Conference on Applications and Advances* (2002), pp. 273–277.

[7] P. Suresh; A.K. Shukla; N. Munichandraiah. "Temperature dependence studies of a.c. impedance of lithium-ion cells". In: *Journal of Applied Electrochemistry (32)* (2002), pp. 267–273.

[8] S. J. Julier; J. K. Uhlmann. "Reduced sigma point filters for the propagation of means and covariances through nonlinear transformations". In: *Proc. Amer. Control Conf.* (2002), pp. 887–892.

[9] S. J. Julier; J. K. Uhlmann. “The Scaled Unscented Transformation”. In: *Proc. Amer. Control Conf.* (2002), pp. 4555–4559.

[10] S. J. Julier. “The Spherical Simplex Unscented Transformation”. In: *Proc. Amer. Control Conf.* (2003), pp. 2430–2434.

[11] Gregory L. Plett. “Extended Kalman filtering for battery management systems of LiPB-based HEV battery pack, Part 2, Modeling and identification”. In: *J. Power Sources* 134 (2004), pp. 262–276.

[12] Gregory L. Plett. “Extended Kalman filtering for battery management systems of LiPB-based HEV battery pack, Part 3, State and parameter estimation”. In: *J. Power Sources* 134 (2004), pp. 277–292.

[13] Van Der Merwe R. “Sigma-Point Kalman Filters for Probabilistic Inference in Dynamic State-Space Models”. (Doctoral dissertation) Oregon Health & Science University, 2004.

[14] J. Vetter et al. “Ageing mechanisms in lithium-ion batteries”. In: *Journal of Power Sources (147)* (2005), pp. 269–281.

[15] B.V. Ratnakumar; M.C. Smart; L.D. Whitcanack; R.C. Ewell. “The impedance characteristics of Mars Exploration Rover Li-ion batteries”. In: *Journal of Power Sources (159)* (2006), pp. 1428–1439.

[16] E. Kuhn; C. Forgez; P. Lagonotte; G. Friedrich. “Modelling Ni-mH battery using Cauer and Foster structures”. In: *Journal of Power Sources (158)* (2006), pp. 1490–1497.

[17] G.L. Plett. “Sigma-point Kalman filtering for battery management systems of LiPB-based HEV battery packs Part 1: Introduction and state estimation”. In: *Journal of Power Sources (161)* (2006), pp. 1356–1368.

[18] G.L. Plett. “Sigma-point Kalman filtering for battery management systems of LiPB-based HEV battery packs Part 2: Simultaneous state and parameter estimation”. In: *Journal of Power Sources (161)* (2006), pp. 1369–1384.

[19] A. Jossen; W. Weydanz. “Moderne Akkumulatoren richtig einsetzen”. In: *Inge Reichardt Verlag* (2006).

[20] M.E. Orazem; B. Tribollet. *“Electrochemical Impedance Spectroscopy”*. Wiley, 2008, pp. 73–96. ISBN: 978-0-470-38158-8.

[21] M.J. Klein G.L. Plett R.A. Jackey. “Parameterization of a Battery Simulation Model Using Numerical Optimization Methods”. In: *SAE Technical Paper 2009-01-1381* (2009). DOI: 10.4271/2009-01-1381.

[22] D.U. Sauer. “Charge–Discharge Curves”. In: *J. Garche et al.(Eds.), Encyclopedia of Electrochemical Power Sources, Elsevier* (2009), pp. 443–451.

[23] R.G. Brown; P.Y.C. Hwang. *Introduction to Random Signals and Applied Kalman Filtering*. Wiley, 2012. ISBN: 9780470609699.

[24] D. H. Doughty; A. A. Pesaran. “Vehicle Battery Safety Roadmap Guidance”. In: *National Renewable Energy Laboratory* (2012).

[25] R. Al Nazer et al. “Broadband Identification of Battery Electrical Impedance for HEVs”. In: *IEEE Transaction on Vehicular Technology* Vol. 62, No. 7 (2013), pp. 2896–2905.

[26] Chao-Yang Wang Christopher D. Rahn. *“Battery Systems Engineering”*. Wiley, Jan. 2013. ISBN: 9781119979500.

[27] C. Dyer; P. Moseley; Z. Ogumi; D. Rand; B. Scrosati; J. Garche. “Encyclopedia of Electrochemical Power Sources”. In: *Elsevier Science* (2013).

[28] G. Pilatowicz. “Anleitungen zum Batteriepraktikum”. In: *Institut für Stromrichtertechnik und elektrische Antriebe* (2013).

[29] A. Thielmann; A. Sauer; R. Isenmann; M. Wietschel; P. Plötz. “Product Roadmap Lithium-ion Batteries 2030”. In: *Fraunhofer Institute for Systems and Innovation Research ISI, Karlsruhe* (2013).

[30] W. Waag; C. Fleischer; D. U. Sauer. “On-line estimation of lithium-ion battery impedance parameters using a novel varied-parameters approach”. In: *Journal of Power Sources (237)* (2013), pp. 260–269.

[31] W. Waag; S. Käbitz; D. U. Sauer. “Experimental investigation of the lithium-ion battery impedance characteristic at various conditions and aging states and its influence on the application”. In: *Applied Energy (102)* (2013), pp. 885–897.

[32] W. Waag; S. Käbitz; D.U. Sauer. “Experimental investigation of the lithium-ion battery impedance characteristic at various conditions and aging states and its influence on the application”. In: *Applied Energy (102)* (2013), pp. 885–897.

[33] A. Thielmann; A. Sauer; R. Isenmann; M. Wietschel. “Technology Roadmap Energy Storage for Electric Mobility 2030”. In: *Fraunhofer Institute for Systems and Innovation Research ISI, Karlsruhe* (2013).

[34] D. A. Howey et al. “Online Measurement of Battery Impedance Using Motor Controller Excitation”. In: *IEEE Transaction on Vehicular Technology* Vol. 63, No. 6 (2014), pp. 2557–2566.

[35] J. de Hoog et al. “Aging phenomena for Lithium-Ion batteries”. In: *European Electric Vehicle Congress* (2014).

[36] C. Fleischer; W. Waag; H-M. Heyn; D.U. Sauer. “On-line adaptive battery impedance parameter and state estimation considering physical principles in reduced order equivalent circuit battery models: Part 1. Requirements, critical review of methods and modeling”. In: *J. Power sources (260)* (2014), pp. 276–291.

[37] C. Fleischer; W. Waag; H-M. Heyn; D.U. Sauer. “On-line adaptive battery impedance parameter and state estimation considering physical principles in reduced order equivalent circuit battery models: Part 2. Parameter and state estimation”. In: *J. Power sources (262)* (2014), pp. 457–482.

[38] W. Waag; C. Fleischer; D. U. Sauer. “Critical review of the methods for monitoring of lithium-ion batteries in electric and hybrid vehicles”. In: *Journal of Power Sources (258)* (2014), pp. 321–339.

[39] A. Baba; S. Adachi. “Simultaneous State Of Charge and Parameter Estimation of Lithium-ion Battery Using Log-normalized Unscented Kalman Filter”. In: *American Control Conference* (2015).

[40] H. Piret et al. “Passive and active tracking of electrochemical impedance of a drone battery”. In: *European Battery, Hybrid and Fuel Cell Electric Vehicle Congress* (2015).

[41] B. Wang; S.E. Li; H. Peng; Z. Liu. “Fractional-order modeling and parameter identification for lithium-ion batteries”. In: *Journal of Power Sources (293)* (2015), pp. 151–161.

[42] Gregory L. Plett. *”Battery Management Systems, Volume I: Battery Modeling”*. Artech House Publishers, 2015. ISBN: 978-1-63081-023-8.

[43] Gregory L. Plett. *“Battery management systems, Volume II: Equivalent-circuit methods”*. Artech House Publishers, 2015. ISBN: 978-1-63081-027-6.

[44] J. Jiang; C. Zhang. *“Fundamentals and Applications of Lithium-ion Batteries in Electric Vehicles”*. Wiley, 2015. ISBN: 978-1-118-41478-1.

[45] C. Julien et al. *“Lithium Batteries – Science and Technology”*. Springer International Publishing, 2016, pp. 16–18. ISBN: 978-3-319-19107-2.

[46] M. Berecibar et al. “Critical review of state of health estimation methods of Li-ion batteries for real applications”. In: *Renewable and Sustainable Energy Reviews (56)* (2016), pp. 572–587.

[47] Project Engineering and Contracting (PEC). *ACT Programmer Manual*. Leuven, Belgium, 2016.

[48] Ø. Gjengedal. “Battery Modeling and Kalman Filter-based State-of-Charge Estimation for a Race Car Application”. In: *Technical Report, Norwegian University of Science and Technology* (2016).

[49] Ø. Gjengedal; M. Molinas; P. J. Svela Vie. “Battery Modeling and Kalman Filter-based State-of-Charge Estimation for a Race Car Application”. In: *14th IEEE International Conference on Networking, Sensing and Control* (Calabria, Italy, 16-18 May, 2017). DOI: 10.1109/ICNSC.2017.8000153.

[50] G.L. Plett. “Efficient Battery Pack State Estimation using Bar-Delta Filtering”. In: *CD-ROM Proc. 24th Electric Vehicle Symposium (EVS24), Stavanger, Norway* (May 2009), pp. 1369–1384.

Appendices

Appendix A

Case-study supplementary

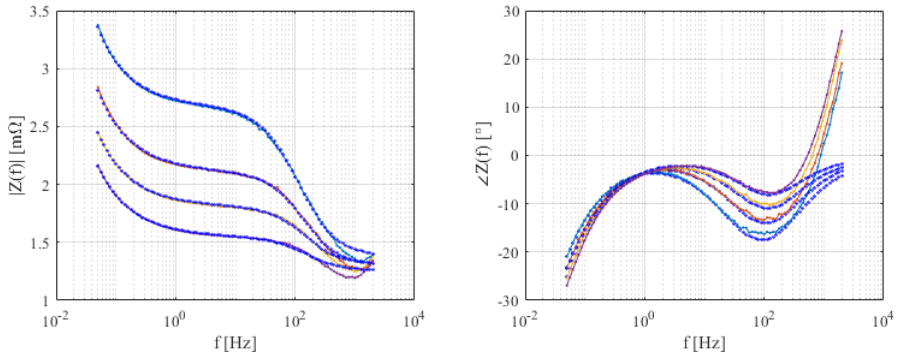

(a) 60% SoC

(b) 3.7% SoC

Figure A.1: Bode plot -Model fitting (dark blue) at two levels of SoC and various temperatures: $25°C$ (light blue), $30°C$ (orange), $35°C$ (yellow), $40°C$ (purple).

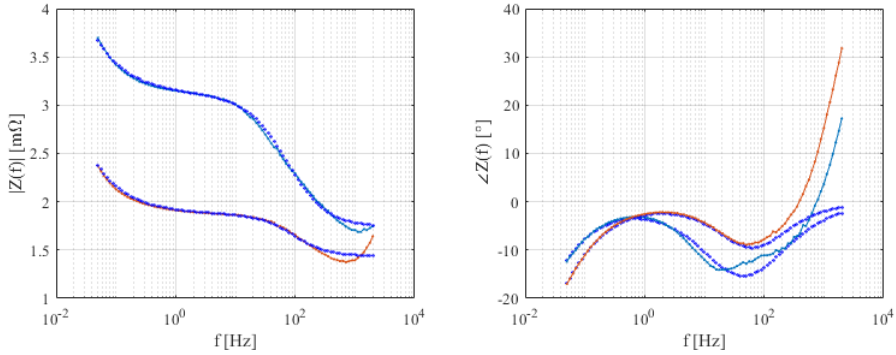

(a) 57% SoC (b) 14% SoC

Figure A.2: Bode plot - Model fitting (dark blue) at two levels of SoC and temperatures: $25°C$ (light blue), $40°C$ (orange).

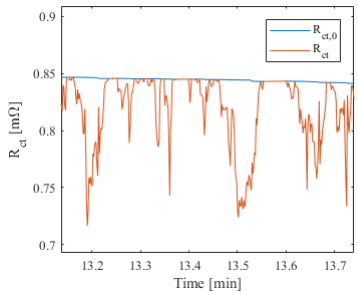

Figure A.3: The behavior of the non-linear charge-transfer model using the proposed method in Chapter 4

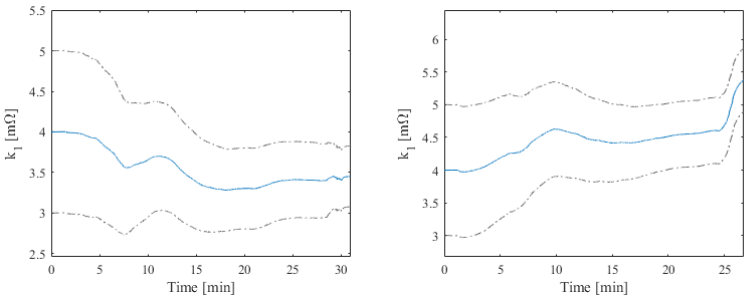

(a) New cell (b) Aged cell

Figure A.4: Diffusion parameter k_1 related to transmissive Warburg impedance.

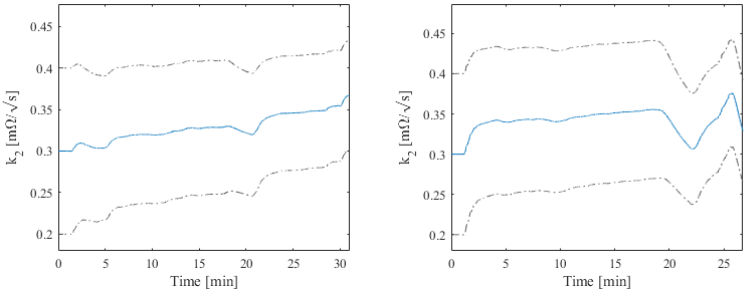

(a) New cell (b) Aged cell

Figure A.5: Diffusion parameter k_2 related to transmissive Warburg impedance.

Appendix B

Cell datasheet

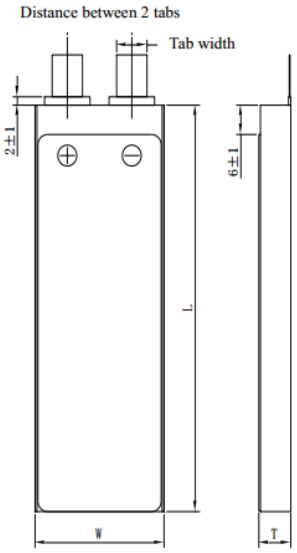

◆标称容量 Typical Capacity①		6.55Ah
◆标称电压 Nominal Voltage		3.7V
◆ 充电条件 Charge Condition	最大电流 Max. Continuous charge Current	13.1A
	峰值充电 Peak charge current	26.2A(≤1sec)
	电压 Voltage	4.2V±0.03V
◆ 放电条件 Discharge Condition	Max Continuous Discharge Current	65.5A
	Peak Discharge Current	98.25A
	Cut-off Voltage	3.0V
◆交流内阻 AC Impedance(mOHM)		<3.0
◆循环寿命【充电:1.0C,放电:10C】 Cycle Life【CHA:1.0C,DCH:10C】		>100cycles
◆使用温度 Operating Temp.	充电 Charge	0℃~45℃
	放电 Discharge	-20℃~60℃
◆ 电芯尺寸 Cell Dimensions	厚度 Thickness(T)	10.7±0.3mm
	宽度 Width(W)	42±0.5mm
	长度 Length(L)	127.5±0.5mm
	极耳间距 Distance between 2 tabs	21±1mm
◆ 极耳尺寸 Dimensions of Cell tabs	极耳宽度 Tab Width	12mm
	极耳厚度 Tab Thickness	0.2mm
	极耳长度 Tab Length	Max 30mm
◆重量 Weight(g)		128.5±3.0
①标称容量：0.5CmA,4.2V~3.0V@23℃±2℃ Typical Capacity:0.5CmA,4.2V~3.0V@23℃±2℃		

Appendix C

EIS at various SoC and temperatures

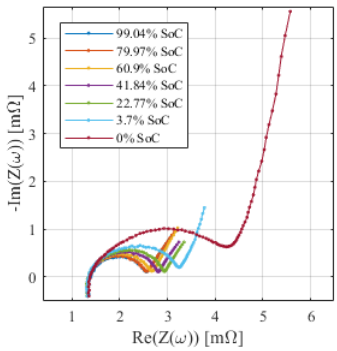

(a) $T = 25°C$

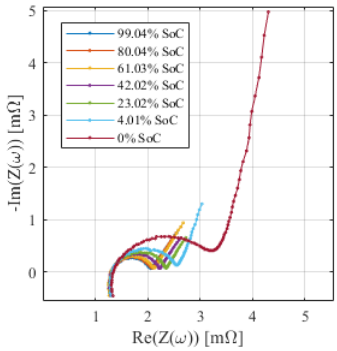

(b) $T = 30°C$

Figure C.1: Nyquist plot of impedance spectra ($f \in [50mHz, 2kHz]$) for the new cell.

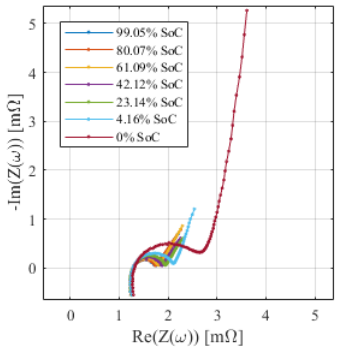

(a) $T = 35°C$

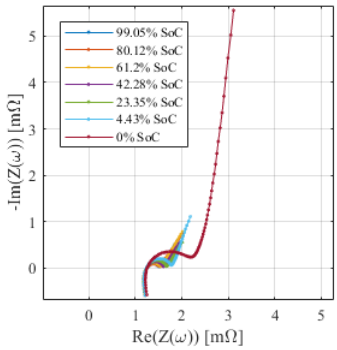

(b) $T = 40°C$

Figure C.2: Nyquist plot of impedance spectra ($f \in [50mHz, 2kHz]$) for the new cell.

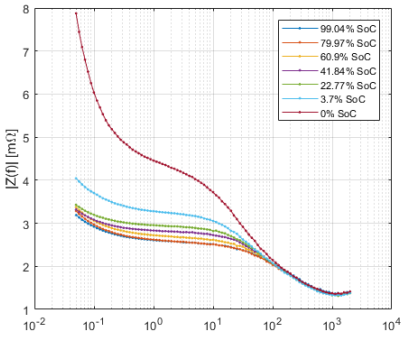

(a) *Magnitude*

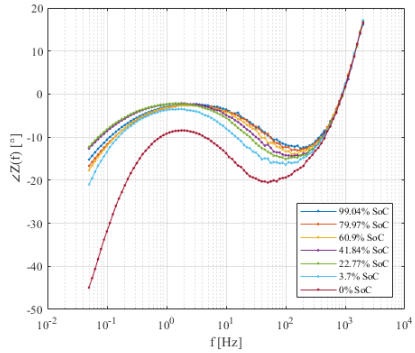

(b) *Phase*

Figure C.3: Bode plot of impedance spectra for the aged cell at $25°C$.

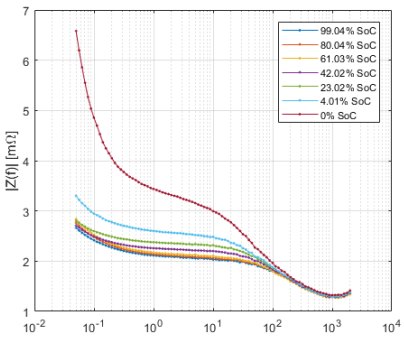

(a) *Magnitude*

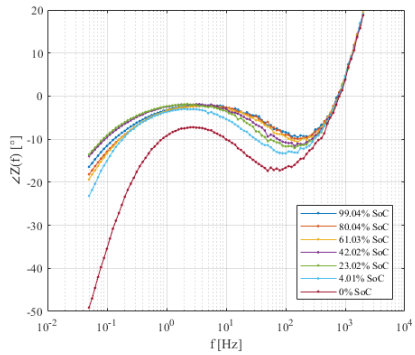

(b) *Phase*

Figure C.4: Bode plot of impedance spectra for the agedaged cell at $30°C$.

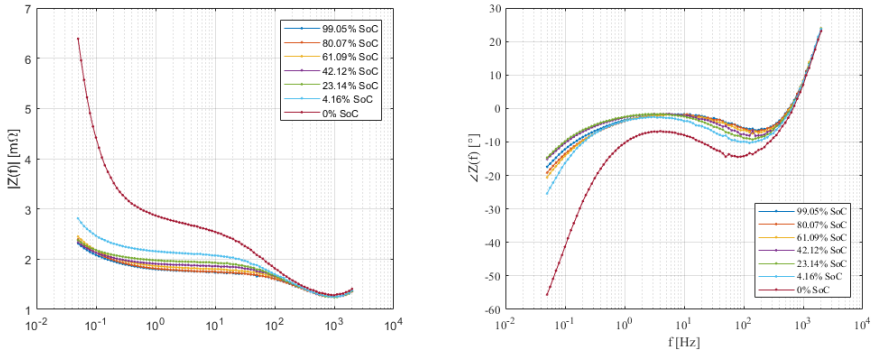

(a) *Magnitude* (b) *Phase*

Figure C.5: Bode plot of impedance spectra for the aged cell at $35°C$.

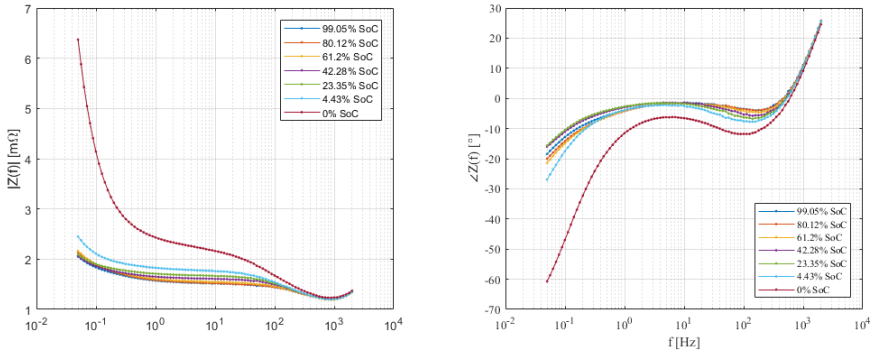

(a) *Magnitude* (b) *Phase*

Figure C.6: Bode plot of impedance spectra for the aged cell at $40°C$.

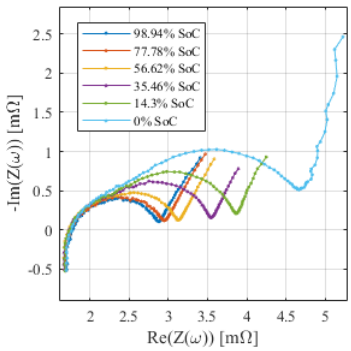

(a) $T = 25°C$

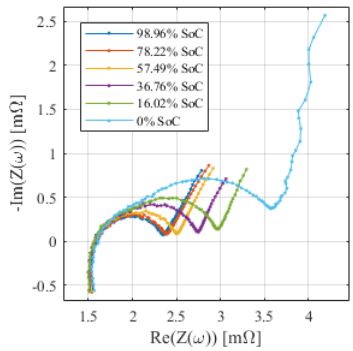

(b) $T = 30°C$

Figure C.7: Nyquist plot of impedance spectra ($f \in [50mHz, 2kHz]$) for the aged cell.

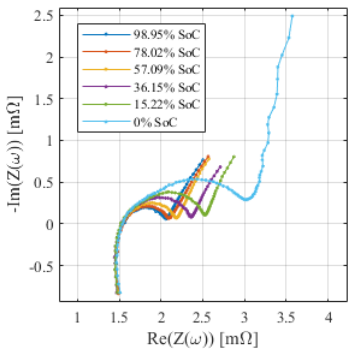

(a) $T = 35°C$

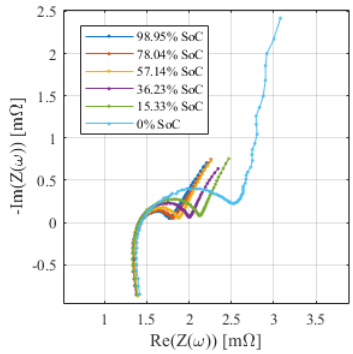

(b) $T = 40°C$

Figure C.8: Nyquist plot of impedance spectra ($f \in [50mHz, 2kHz]$) for the aged cell.

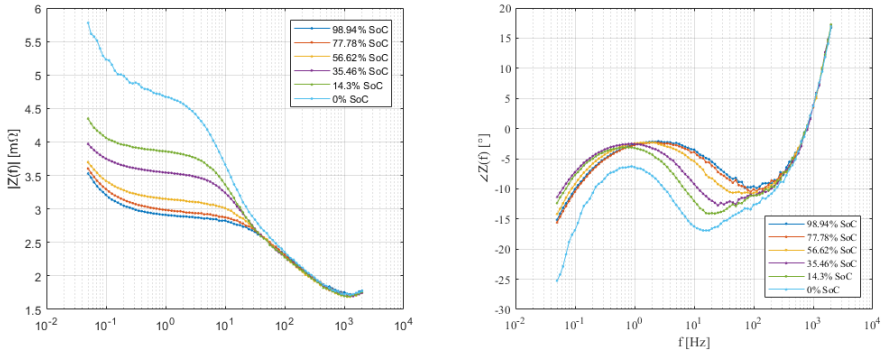

(a) *Magnitude* (b) *Phase*

Figure C.9: Bode plot of impedance spectra for the aged cell at $25°C$.

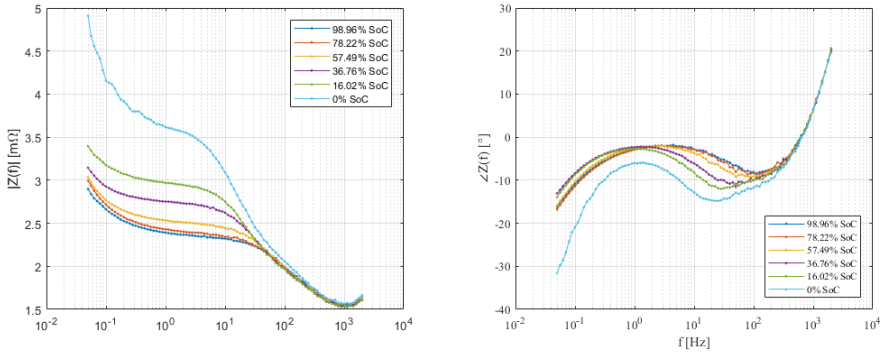

(a) *Magnitude* (b) *Phase*

Figure C.10: Bode plot of impedance spectra for the aged cell at $30°C$.

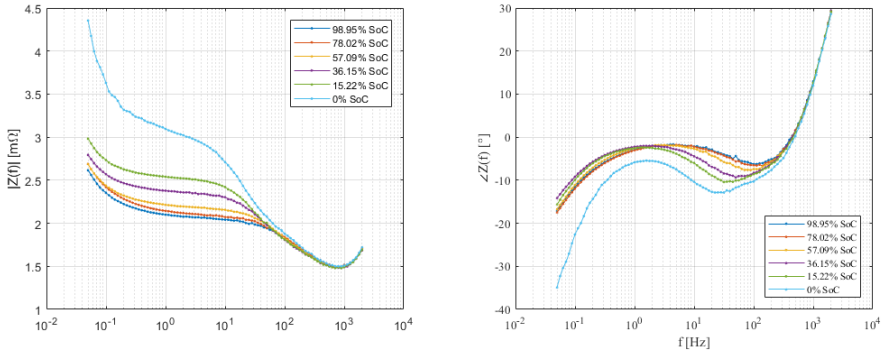

(a) *Magnitude* (b) *Phase*

Figure C.11: Bode plot of impedance spectra for the aged cell at $35°C$.

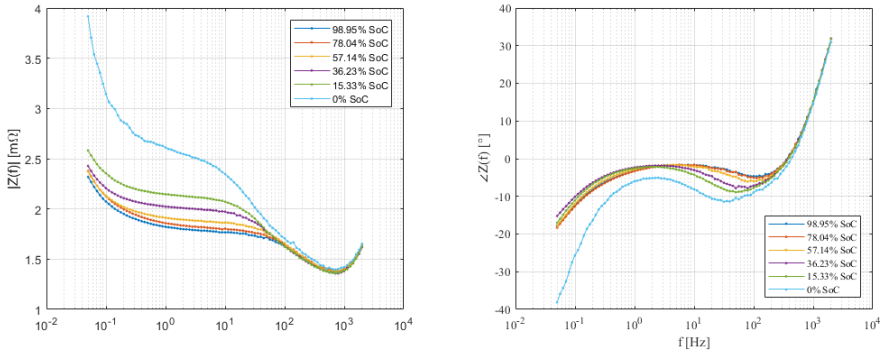

(a) *Magnitude* (b) *Phase*

Figure C.12: Bode plot of impedance spectra for the aged cell at $40°C$.